Global Biogeochemical Cycles

RESEARCH ARTICLE
10.1029/2024GB008243

Special Collection:
The U.S. GEOTRACES Pacific Meridional Transect (GP15)

^{210}Po and ^{210}Pb Distributions Along the GEOTRACES Pacific Meridional Transect (GP15): Tracers of Scavenging and Particulate Organic Carbon (POC) Export

J. Kirk Cochran[1], Ziran Wei[1,2], Evan Horowitz[1], Patrick Fitzgerald[1], Christina Heilbrun[1], Mark Stephens[3], Phoebe J. Lam[4], Emilie Le Roy[5,6], and Matthew Charette[5]

[1]School of Marine & Atmospheric Sciences, Stony Brook University, Stony Brook, NY, USA, [2]Now at Department of Oceanography and Coastal Sciences, Louisiana State University, Baton Rouge, LA, USA, [3]Florida International University, Applied Research Center, Miami, FL, USA, [4]Department of Ocean Sciences, University of California-Santa Cruz, Santa Cruz, CA, USA, [5]Department of Marine Chemistry and Geochemistry, Woods Hole Oceanographic Institution, Woods Hole, MA, USA, [6]Now at CNRS, IRD, Ifremer, UMR, LEMAR, University of Brest, Plouzane, France

Abstract Distributions of the natural radionuclide ^{210}Po and its grandparent ^{210}Pb along the GP15 Pacific Meridional Transect provide information on scavenging rates of reactive chemical species throughout the water column and fluxes of particulate organic carbon (POC) from the primary production zone (PPZ). ^{210}Pb is in excess of its grandparent ^{226}Ra in the upper 400–700 m due to the atmospheric flux of ^{210}Pb. Mid-water ^{210}Pb/^{226}Ra activity ratios are close to radioactive equilibrium (1.0) north of ~20°N, indicating slow scavenging, but deficiencies at stations near and south of the equator suggest more rapid scavenging associated with a "particle veil" located at the equator and hydrothermal processes at the East Pacific Rise. Scavenging of ^{210}Pb and ^{210}Po is evident in the bottom 500–1,000 m at most stations due to enhanced removal in the nepheloid layer. Deficits in the PPZ of ^{210}Po (relative to ^{210}Pb) and ^{210}Pb (relative to ^{226}Ra decay and the ^{210}Pb atmospheric flux), together with POC concentrations and particulate ^{210}Po and ^{210}Pb activities, are used to calculate export fluxes of POC from the PPZ. ^{210}Po-derived POC fluxes on large (>51 μm) particles range from 15.5 ± 1.3 mmol C/m^2/d to 1.5 ± 0.2 mmol C/m^2/d and are highest in the Subarctic North Pacific; ^{210}Pb-derived fluxes range from 6.7 ± 1.8 mmol C/m^2/d to 0.2 ± 0.1 mmol C/m^2/d. Both ^{210}Po- and ^{210}Pb-derived POC fluxes are greater than those calculated using the ^{234}Th proxy, possibly due to different integration times of the radionuclides, considering their different radioactive mean-lives and scavenging mean residence times.

Key Points:
- ^{210}Po and ^{210}Pb distributions along 152°W yield scavenging rates and fluxes of particulate organic carbon (POC) from the water column
- Residence times of ^{210}Pb with respect to scavenging in the primary production zone (PPZ) are 0.8 to 15 y. Values for ^{210}Po are 0.2–0.5 y
- Export of POC from the PPZ ranges from 15.5 to 1.5 mmol C/m^2/d using ^{210}Po and 6.7 to 0.2 mmol C/m^2/d using ^{210}Pb

Supporting Information:
Supporting Information may be found in the online version of this article.

Correspondence to:
J. K. Cochran,
kirk.cochran@stonybrook.edu

Citation:
Cochran, J. K., Wei, Z., Horowitz, E., Fitzgerald, P., Heilbrun, C., Stephens, M., et al. (2024). ^{210}Po and ^{210}Pb distributions along the GEOTRACES Pacific Meridional Transect (GP15): Tracers of scavenging and particulate organic carbon (POC) export. *Global Biogeochemical Cycles*, *38*, e2024GB008243. https://doi.org/10.1029/2024GB008243

Received 28 MAY 2024
Accepted 8 OCT 2024

Author Contributions:
Conceptualization: J. Kirk Cochran, Ziran Wei, Evan Horowitz, Patrick Fitzgerald, Matthew Charette
Data curation: J. Kirk Cochran, Ziran Wei, Evan Horowitz, Patrick Fitzgerald, Christina Heilbrun, Mark Stephens
Formal analysis: J. Kirk Cochran, Ziran Wei, Evan Horowitz, Patrick Fitzgerald, Mark Stephens
Funding acquisition: J. Kirk Cochran, Mark Stephens, Phoebe J. Lam, Matthew Charette
Investigation: J. Kirk Cochran, Ziran Wei, Evan Horowitz, Patrick Fitzgerald,

1. Introduction

Natural radionuclides of the U-and Th-decay series have proved very useful in studying ocean processes, including, but certainly not limited to, understanding the mechanisms and rates of scavenging of particle-reactive trace elements. Polonium-210 (^{210}Po: half-life = 138.4 days) and its grandparent, lead-210 (^{210}Pb: half-life = 22.3 years), both members of the ^{238}U decay series, are considered particle-reactive in their respective marine geochemistries, and their oceanic distributions have been studied for over 60 years (e.g., Bacon et al., 1976; Chung & Craig, 1983; Chung & Wu, 2005; Craig et al., 1973; Kim & Church, 2001; Nozaki et al., 1976; Rama et al., 1961; Somayajulu & Craig, 1976; Spencer et al., 1981; Thomson & Turekian, 1976; Tsunogai & Nozaki, 1971). ^{210}Po in seawater is produced predominantly through the decay of ^{210}Pb (via the 5-day half-life intermediate ^{210}Bi). ^{210}Pb is produced ultimately from decay of its grandparent, dissolved ^{226}Ra, and is also added to the surface ocean from the atmosphere, where it is produced by the decay of ^{222}Rn that has emanated principally from continental rocks and soils. The ^{222}Rn flux from continental rocks and soils is much greater than that from the surface ocean, and consequently, the ^{210}Pb flux to the Earth's surface is generally higher over the continents than over the ocean.

Early results documenting distributions of ^{210}Po and ^{210}Pb in the oceans (Bacon et al., 1976, 1988; Chung & Finkel, 1988; Cochran et al., 1983; Nozaki & Tsunogai, 1976; Nozaki et al., 1976; Thomson & Turekian, 1976; Tsunogai & Nozaki, 1971; see also Cochran, 1992) showed that ^{210}Pb was scavenged relative to radioactive equilibrium with its grandparent ^{226}Ra and that ^{210}Po was more rapidly removed from surface waters than ^{210}Pb (activity ratio ^{210}Po/^{210}Pb in solution <1). At depth, however, ^{210}Po can be released from sinking particles such that the activity ratio of ^{210}Po/^{210}Pb in solution is more than 1 (Bacon et al., 1988; Cochran, 1992; Cochran et al., 1983). Excess ^{210}Po has also been observed in surface waters within upwelled coastal filaments as the

Mark Stephens, Phoebe J. Lam, Matthew Charette
Methodology: J. Kirk Cochran, Ziran Wei, Evan Horowitz, Patrick Fitzgerald, Christina Heilbrun, Mark Stephens, Phoebe J. Lam, Emilie Le Roy, Matthew Charette
Project administration: J. Kirk Cochran, Christina Heilbrun
Resources: J. Kirk Cochran, Mark Stephens, Phoebe J. Lam, Emilie Le Roy
Software: Ziran Wei, Evan Horowitz, Christina Heilbrun
Supervision: J. Kirk Cochran
Validation: J. Kirk Cochran, Ziran Wei, Evan Horowitz, Patrick Fitzgerald, Christina Heilbrun, Mark Stephens
Visualization: J. Kirk Cochran, Ziran Wei, Evan Horowitz
Writing – original draft: J. Kirk Cochran, Ziran Wei, Evan Horowitz, Phoebe J. Lam, Emilie Le Roy, Matthew Charette
Writing – review & editing: J. Kirk Cochran, Ziran Wei, Mark Stephens, Phoebe J. Lam, Emilie Le Roy, Matthew Charette

products of particle respiration (e.g., NO_3^-, NO_2^-) are transported upward by the upwelling process (Kadko, 1993).

An important aspect of the behavior of Po that helps explain these observations of $^{210}Po/^{210}Pb$ disequilibrium is its assimilation into cells, possibly as an analog of sulfur (Fisher et al., 1983, 1987). Stewart and Fisher (2003a, 2003b) showed that Po uptake in marine phytoplankton cultured in the laboratory comprised both a surface-bound fraction and a cellular fraction associated with protein. Indeed, 30%–60% of the total Po was present in the cytoplasm. Such behavior helps account for the observed links between chlorophyll a (denoting living organic matter), productivity, particulate carbon concentration (POC) and the rate of Po scavenging (Choi et al., 2014; Hong et al., 1999; Nozaki et al., 1997, 1998; Sarin et al., 1999). The Po assimilated into the cytoplasm by phytoplankton may be released as the organic matter decomposes during sinking. Thus, Po may behave more like carbon than Th or Pb with respect to its scavenging on particulate organic matter and involvement in marine food webs. This aspect makes it a potentially powerful tracer of POC export, in a complementary fashion to the use of ^{234}Th as a POC flux proxy (e.g., Buesseler et al., 1992).

The export and fate of sinking POC through the mesopelagic are critical to understanding the efficiency of the biological pump and, ultimately, its control of atmospheric CO_2 (Passow & Carlson, 2012). $^{234}Th/^{238}U$ and $^{210}Po/^{210}Pb$ disequilibria (and other radionuclide proxies of POC and particle flux; Hayes et al., 2018) have increasingly been used in this manner (Anand et al., 2018; Buesseler et al., 1992; Buesseler, Benitez-Nelson, et al., 2020; Ceballos-Romero et al., 2016; Friedrich & Rutgers van der Loeff, 2002; Horowitz et al., 2020; Lemaitre et al., 2018; LeMoigne et al., 2013; Nozaki et al., 1997; Owens et al., 2015; Roca-Martí et al., 2016; Shimmield et al., 1995; Stewart et al., 2007, 2010; Verdeny et al., 2009). Both the $^{234}Th/^{238}U$ and $^{210}Po/^{210}Pb$ proxies rely on the fact that the daughter nuclide is more particle more reactive than the parent and thus is scavenged preferentially. In the upper ocean, scavenging is often mediated by the biogenic production and sinking of particles, and thus the deficit in the daughter radionuclide relative to radioactive equilibrium with the parent can be converted to a radionuclide flux, and ultimately into a POC flux if the ratio of POC to daughter radionuclide on sinking particles is known. The half-lives of ^{234}Th and ^{210}Po are significantly different– 24.1 days for ^{234}Th and 138.4 days for ^{210}Po– suggesting that they integrate export over different time scales. These radionuclide POC-flux proxies serve as complements to each other and to other approaches such as measurements of nutrient cycling and balances as well as deployment of sediment traps (Buesseler et al., 2007) and are especially useful in cases where the latter (i.e., traps) cannot be readily used due to logistical constraints.

The GEOTRACES Pacific Meridional Transect cruise (GP15) was carried out in 2018 (09/18–11/25/2018) along 152°W from Alaska to Tahiti (Figure 1). The cruise was divided into two legs. Leg 1, designated RR1814, ran from 9/18–10/21/2018 and included stations 1–18.3. Leg 2, designated RR1815, ran from 10/25–11/24/2018 and included stations 18.6 to 39. At its northern end, the cruise sampled the shelf/slope in the interior Gulf of Alaska. The transect crossed numerous biogeochemical "provinces," including the relatively productive region of the eastern subarctic Pacific and the high productivity Subarctic Frontal Zone at 42°N, the oligotrophic North Pacific subtropical gyre, the productive equatorial region, and the highly oligotrophic South Pacific subtropical gyre (Figure 2). The transect also intersected hydrothermal plumes extending from the Juan de Fuca Ridge (35°N), Loihi Seamount (19°N), and the East Pacific Rise (EPR) (9°N, 15°S). Here we report the activities of ^{210}Po and ^{210}Pb in the dissolved and particulate fractions of water samples collected on GP15. Our goal is to use these radionuclides as coupled and single tracers of scavenging rates and POC export along the transect.

2. Materials and Methods

2.1. Dissolved Samples

Water samples for ^{210}Po and ^{210}Pb were collected at 12 stations along the GP15 transect (Figure 1) and processed on board through the initial plating of Po. Surface water (~3 m) was collected using a towed GeoFish sampler designed to collect trace-metal clean near-surface water samples (https://www.bco-dmo.org/instrument/549). These samples (10L) were not filtered (so they represent total activities of ^{210}Po and ^{210}Pb) but were acidified with HCl soon after collection. For dissolved activities, samples (10L) were collected using the Scripps Ocean Data Facility (ODF) rosette. Samples were filtered through Acropak filter cartridges (0.8 μm/0.45 μm) and acidified to pH ~2 with 40 mL of 6N HCl. They were then shaken well to homogenize. Iron (10 mg Fe, as $FeCl_3$ solution) was added along with 10 mg of stable Pb carrier (in 2N HNO_3) and 1.76 dpm of ^{209}Po tracer (in 2N HNO_3; National Institute of Standards and Technology 4326a). The mixture was shaken and left for 24 hr for tracer/carrier

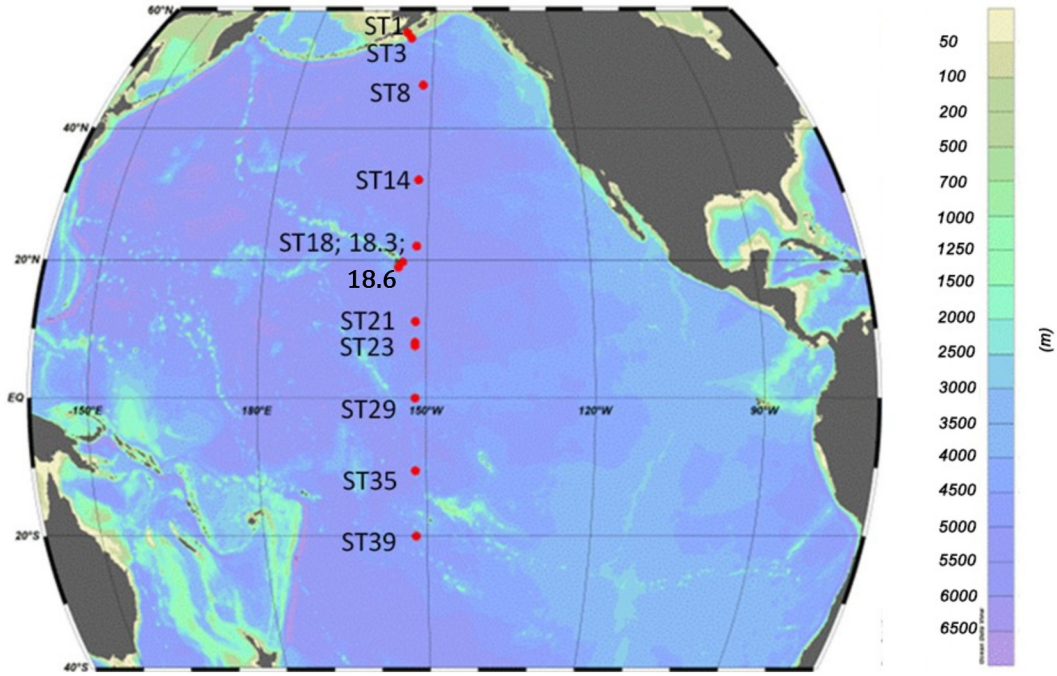

Figure 1. Map of the GEOTRACES GP15 Pacific Meridional Transect showing stations sampled for ^{210}Po and ^{210}Pb. Stations 1 and 3 are on the Alaska shelf and slope; Stations 8–39 are along 152°W. Station 18.3 sampled the Puna Ridge and nearby station 18.6 sampled the Loihi Seamount. Water depth contours (m) are scaled at right.

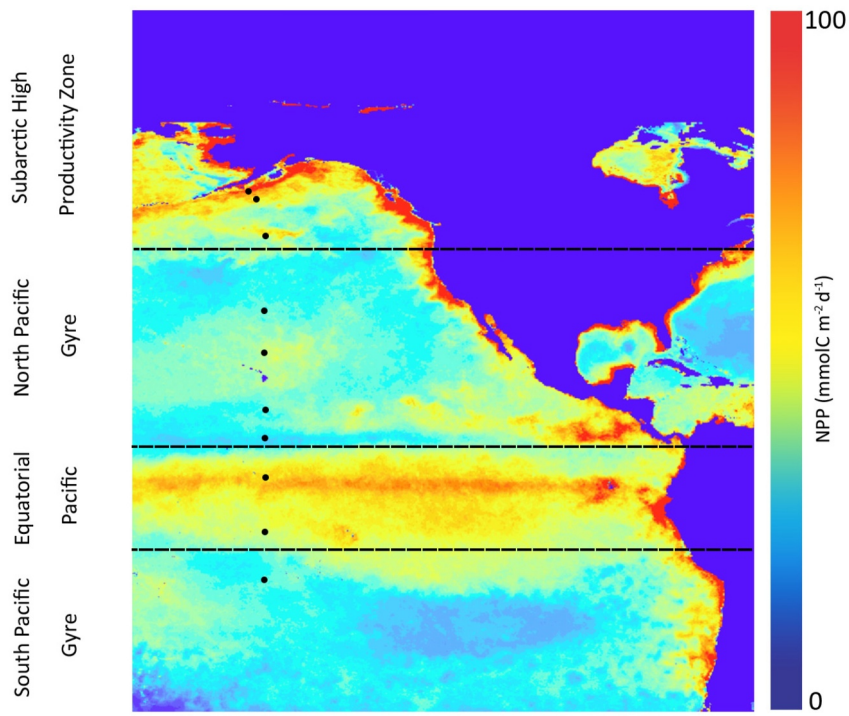

Figure 2. Net primary production along the GP15 transect integrated over the prior 6 months of the cruise. Recalculated and plotted using ArcGIS from the MODIS r2018 satellite product collated by the monthly CbPM HDF files by Oregon State University Ocean Productivity (Westberry et al., 2008). Retrieved from http://orca.science.oregonstate.edu/1080.by.2160.monthly.hdf.cbpm2.m.php. Boundaries designated by horizontal dashed lines are: Subarctic- north of ~47°N; North Pacific- ~7°–47°N; Equatorial- ~7°N–12°S; South Pacific-south of 12°S (Kenyon, 2022).

equilibration. Iron hydroxide was precipitated by adding concentrated NH_4OH to raise the pH to 8–9. The Fe $(OH)_3$ precipitate was allowed to settle for 24 hr after which the sample was filtered through a 142 mm diameter 1.2 μm Versapor filter. The precipitate was dissolved in 20 mL of 6N HCl, and the solution was diluted with DI water to make 80 mL of 1.5 N HCl. Ascorbic acid was added to the 1.5 N HCl solution and polonium was plated onto silver planchets (Flynn, 1968; Lee et al., 2014) mounted in Teflon planchet-holders fitted with magnetic stir bars. Plating proceeded on magnetic-stirrer hot plates heated to 80°C for 3 hr. Planchets were then removed from the solution, rinsed, and allowed to dry. Dried Po-plated planchets were returned to the shore-based laboratories (Stony Brook University; Florida International University) for alpha counting.

The residual plating solutions were transferred to 125 mL polycarbonate bottles for transport back to Stony Brook University. Due to the long transit back from the Pacific (~3 months), it was decided to eliminate any residual ^{209}Po and ^{210}Po left in the sample after plating by suspending a piece of scrap silver (~0.5 g) in the sample for 5 days at sea. The silver was then removed with the time of removal noted. This clean-up step was checked upon sample return to the laboratory by replating several samples without any additional ^{209}Po added. We found that 5.0% ± 1.6% of the initial Po remained, and correction was made to the calculation of ^{210}Pb activities to account for residual ^{210}Po and ^{209}Po. Additionally, to check the clean-up procedure, two samples were purified by ion exchange after their return to the lab. The agreement was within 6% (within counting error), indicating that the clean-up step using scrap silver was sufficient. An additional aliquot of ^{209}Po was added to the stored samples, and after ~6 months of storage, Po was plated again using the procedure described above. Determination of the recovery of Pb from precipitation through storage is described below.

Activities of ^{226}Ra were determined on 15–25 L water samples using methods described by Charette et al. (2015). Middepth and deep samples were collected using Niskin bottles deployed on in situ pumps (Section 2.2; Charette & Moore, 2023a, 2023b), while shallow samples were taken on water casts with the ODF rosette. Briefly, the samples underwent gravity filtration (~0.5 L/min) through MnO_2 acrylic fiber to remove Ra from seawater, followed by rinsing with deionized water, partial drying, and placement in a sealed fiber holder; the holder was flushed with He and held for at least 5 days before analysis via ^{222}Rn ingrowth and scintillation counting.

2.2. Particulate Samples

Particulate samples were collected by McLane in situ pumps at approximately the same depths as the water samples but on different casts and were analyzed separately. Due to the equipment limitations and potential hazards when doing acid digestions at sea, on-board treatment was not possible for these samples. Two particle sizes were collected by pumping: a large particle fraction collected on a 142 mm 51 μm-polyester mesh prefilter (Sefar 07–51/33) underlain with a 150 μm-polyester mesh filter (Sefar 07–150/41) and a small particle fraction collected on paired 0.8 μm polyethersulfone Pall Supor800 membrane filters (Lam et al., 2015). Several blank and backing filters were also analyzed. The filters were dried on board in a laminar flow hood, split, and placed in a KNF Flexpak Cleanroom polyethylene bag. Aliquots sent to Stony Brook comprised 28–280 L (average ~100 L) filtered for the small particle fraction and 60–330L (average ~250 L) for the large particle fraction. Filter aliquots from Leg 1 were sent to the lab during the port stop in Hilo, HI on 21 October 2018. Leg 2 filters were sent back from Papeete, Tahiti at the conclusion of the cruise on 24 November 2018. Once the filters arrived, they were placed in microwave digestion vessels and spiked with ^{209}Po tracer (1.76 dpm) and 10 mg stable Pb as for the dissolved samples. Concentrated HCl, HNO_3, and HF (5 mL each) were then added to the vessel. The mixture was microwave-digested for 1 hr at 180°C. After digestion, the resulting solution was decanted into a 25 mL Falcon tube, and the digestion vessels were rinsed with small aliquots of DI water. The Falcon tubes were centrifuged and the supernatant pipetted into 50 mL Teflon beakers. The beakers were heated to almost complete dryness before 10 mL of concentrated HCl was added. This process was repeated to ensure that HCl was the only acid present. Then 20 mL of 6 M HCl was added, the solution was decanted into a glass beaker and the Teflon beaker was rinsed with two aliquots of 30 mL DI water. Ascorbic acid was added to the solution to reduce any Fe(III) to Fe(II) and prevent its plating. A silver planchet embedded in a Teflon stirring magnet was added to each of the sample solutions, and the samples were plated at 80°C for 3 hr, then rinsed with DI water and acetone, dried, and counted in the alpha spectrometer to determine the initial ^{210}Po. As described for water samples, residual Po was removed from the solution by adding scrap silver for ~5 days and then transferring the samples to 125 ml polycarbonate bottles for storage and ingrowth of additional ^{210}Po. The second plating was carried out after ~6 months of storage as described for the water samples.

2.3. Determination of Pb Recoveries

Recovery of the Pb carrier added to the samples before precipitation (water samples) or dissolution (particle and aerosol samples) was determined after the initial ^{210}Po plating. For this purpose, an aliquot of each stored solution was taken for total Pb yield by Atomic Absorption Spectroscopy or Inductively Coupled-Plasma Mass Spectroscopy. Recoveries were measured for all water samples and ranged from 44% to 99%. Processing of the particulate samples lagged that of the water samples and recoveries were not completed before the Covid pandemic closed the laboratories at Stony Brook University for an extended period in 2020. After the laboratory reopening, instrumentation problems further delayed measurements. When measurements finally resumed, it was apparent that Pb had been lost from the aliquots taken after initial Po plating. We decided to apply average recoveries obtained before the lab closure to all the particulate samples: 96 ± 3% (n = 36) for the small particles and 91 ± 8% (n = 36) for the large particles. The high recoveries were consistent with complete dissolution of the sample during microwave digestion and minimal subsequent processing.

2.4. Data Reduction

Activities for both ^{210}Po and ^{210}Pb were calculated following the method of Rigaud et al. (2013). Planchets were counted on PIPS alpha detectors using a Canberra Alpha Analyst system. Peak areas were calculated for the ^{209}Po and ^{210}Po peaks to obtain counts per minute (cpm) and detector backgrounds were subtracted. The ingrown ^{210}Po activity was corrected for residual ^{210}Po and ^{209}Po (5.0% ± 1.6%) left after the purification by scrap silver.

Blanks were run for each sample type. For water samples, these included all reagents used in the $Fe(OH)_3$ precipitation. For the particles, these involve analyses of blank filters and reagents used. The ^{210}Pb blank for the particles was larger than the ^{210}Po blank for each filter type (Table S1 in Supporting Information S1). We attribute this to the samples picking up additional ^{210}Po activity during storage, likely from the containers used for storage. In all cases, the blank activities for ^{210}Pb were <5% for dissolved and <20% for particulate samples. Corresponding values for ^{210}Po were <20% for dissolved and <7% for particulate samples.

Errors were propagated using standard error propagation formulas (Rigaud et al., 2013) and included counting errors on sample, background and blank activities, spiking errors, weighing errors (for water samples), and uncertainty of the ^{209}Po tracer activity.

2.5. Intercalibration

Our results were intercalibrated with ^{210}Po and ^{210}Pb profiles determined on other cruises. For ^{210}Pb, it was possible to compare our results (GP15 station 14) with those obtained on the GEOSECS Pacific expedition (station 212) in 1973 (Nozaki et al., 1980). THE GEOSECS samples were mostly filtered library samples, and the comparison with our dissolved data was excellent despite the 45-year gap between the samplings (Figure S1 in Supporting Information S1). It was also possible to compare our dissolved ^{210}Po and ^{210}Pb at station GP15-35 with a crossover station (station 36) sampled in 2013 on GP16, the GEOTRACES Pacific Zonal Transect (Niedermiller & Baskaran, 2019). Here the comparison in activities is acceptable for ^{210}Pb (within about 10%) but less good for ^{210}Po (within about 20%; Figures S2 and S3 in Supporting Information S1). One possible reason for the poorer agreement in dissolved ^{210}Po is related to differences in sample processing. Our samples were processed through the initial Po plating within ∼5 days of sample collection, while the GP16 samples were taken, acidified and shipped back to the shore-based laboratory for processing. The gap between sampling and processing those samples was 3–4 months (Niedermiller, 2017). Roca-Martí et al. (2021) recently hypothesized that because Po can be incorporated into organic matter and cycled with it (Fisher et al., 1983; Stewart & Fisher 2003a, 2003b; Stewart et al., 2005), a fraction of ^{210}Po can be speciated, likely with organic ligands, in such a way that rapid precipitation with $Fe(OH)_3$ after sampling does not extract all ^{210}Po from the sample. Long storage of a sample under acidified conditions before processing allows the speciation to break down, and all the ^{210}Po in the sample is then extracted when $Fe(OH)_3$ is precipitated. If this hypothesis holds, the ^{210}Po values determined on GP15 may be too low, especially in the upper water column, where the biological cycling of Po is highest. Further studies to evaluate this possibility are presently underway. Comparison of the particulate data from GP15-35 and GP16-36 is shown in Figure S4 in Supporting Information S1.

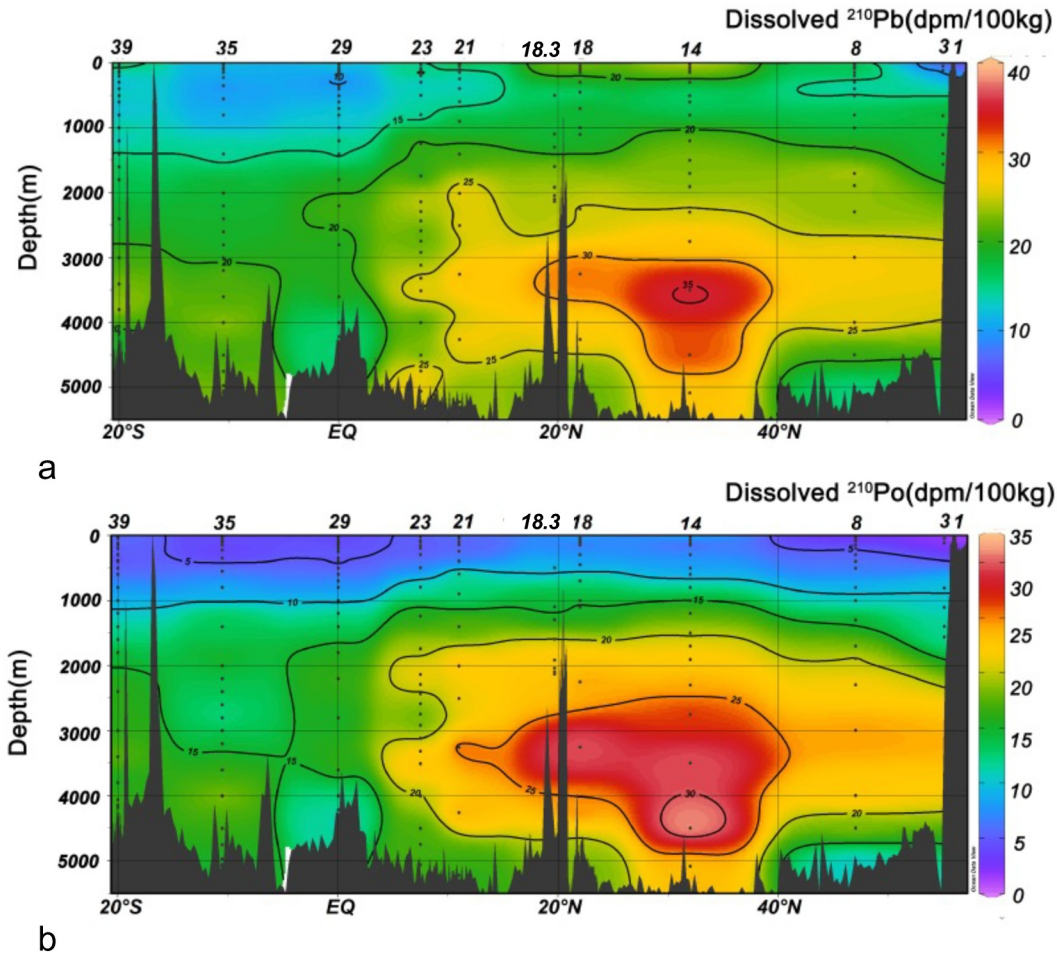

Figure 3. Dissolved (a) ^{210}Pb and (b) ^{210}Po activities (dpm/100 kg) along the GP15 transect.

3. Results

3.1. Water Samples

3.1.1. Dissolved Activities

Activities of dissolved ^{210}Pb ranged from 1.1 dpm/100 kg on the Alaskan shelf to 35.4 dpm/100 kg in the oligotrophic North Pacific (Table S2 in Supporting Information S1; Figure 3a, Cochran & Stephens, 2023a, 2023b). Dissolved ^{210}Pb activities were generally high near the surface (upper 200 m), decreased to a minimum at around 500 m, increased to a maximum between 2,000 and 3,500 m and decreased again in the bottom nepheloid layer. This trend is consistent for the North Pacific stations and is especially seen at station 14, where ^{210}Pb activities peaked at 35.4 dpm/100 kg at 3,500 m depth. South of the North Pacific gyre (stations 29, 35, and 39), such a trend persists but is less clear because the overall ^{210}Pb activities decrease.

Dissolved ^{210}Po ranged from 0.6 to 31.5 dpm/100 kg over the same environments (Figure 3b). In the upper ~800–1,000 m, ^{210}Po shows deficits relative to ^{210}Pb, but at deeper depths, the two radionuclides largely track one another.

3.1.2. Particulate Activities

For both ^{210}Pb and ^{210}Po, dissolved and particulate activities were consistently ranked as dissolved activity >> small particle activity > large particle activity (Data Set S1, Cochran & Stephens, 2023c, 2023d). Total particulate (small + large) ^{210}Po activities exceeded those of ^{210}Pb at most stations (Figures 4a and 4b). In general, total particulate ^{210}Po was less than 10% of the total activity (particulate + dissolved), although it ranged up to

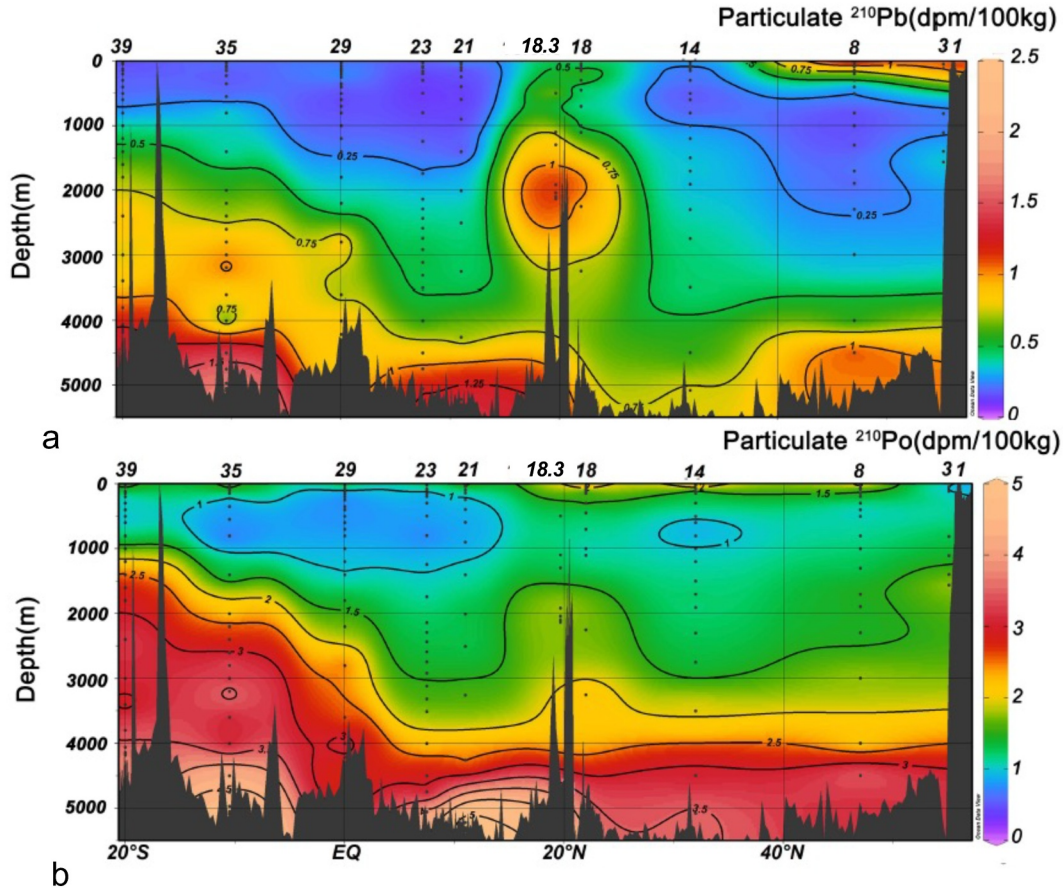

Figure 4. Total particulate (>0.8 μm) (a) ^{210}Pb and (b) ^{210}Po activities (dpm/100 kg) along the GP15 transect.

~60% in near-surface (<50 m) waters and to ~30% in the benthic nepheloid layer. Total particulate ^{210}Pb activities were less than 7% of the total activity, but as with ^{210}Po, showed higher values (up to ~17%) in near-surface waters. At station 1 on the Alaska shelf, particulate activities for both ^{210}Po and ^{210}Pb were high, ~30% to 60% of the total, consistent with higher particle concentrations in that setting.

Although backing filters were supplied with each filter type (see Section 2.2), only a few of these could be analyzed, given time constraints. On average (n = 5), the 150 μm backing filters in the large particle fraction comprised 30% ± 7% of ^{210}Po and 48% ± 13% of ^{210}Pb activities in the top 51 μm filter. The ^{210}Po/^{210}Pb activity ratio on the backing filter was comparable to or greater than that of the top 51 μm filter, indicating that the likely source of ^{210}Po and ^{210}Pb on the backing filter was particles that were not retained by the top filter but were captured by the backing filter. For the small particle fraction (n = 6), the backing Supor800 filter retained 15% ± 10% of the ^{210}Po and 7% ± 5% of the ^{210}Pb in the small particle fraction. The ^{210}Po/^{210}Pb activity ratio on the backing filter was typically significantly greater than that in the top filter. Rather than particle breakthrough, it was likely that some dissolved ^{210}Po and ^{210}Pb adsorbed on the Supor800 filters, with preferential adsorption of ^{210}Po. Taken together, these interpretations suggest that the large particle activities based on the top 51-μm mesh filter could be underestimated by ~40%, and the small particle activities determined from the top Supor800 filters could be overestimated by ~10% for ^{210}Po and ^{210}Pb. However, because of the ranking of activities cited above (dissolved >> small particle > large particle), the patterns in total ^{210}Po and ^{210}Pb activities obtained by summing the fractions are not significantly altered by these constraints on the particulate activities.

3.1.3. Total Activities and Radioactive Disequilibrium

As noted above, except for the surface water samples collected by the GeoFish (unfiltered samples), total activities were calculated by summing the two particulate fractions and the dissolved fraction. The particulate

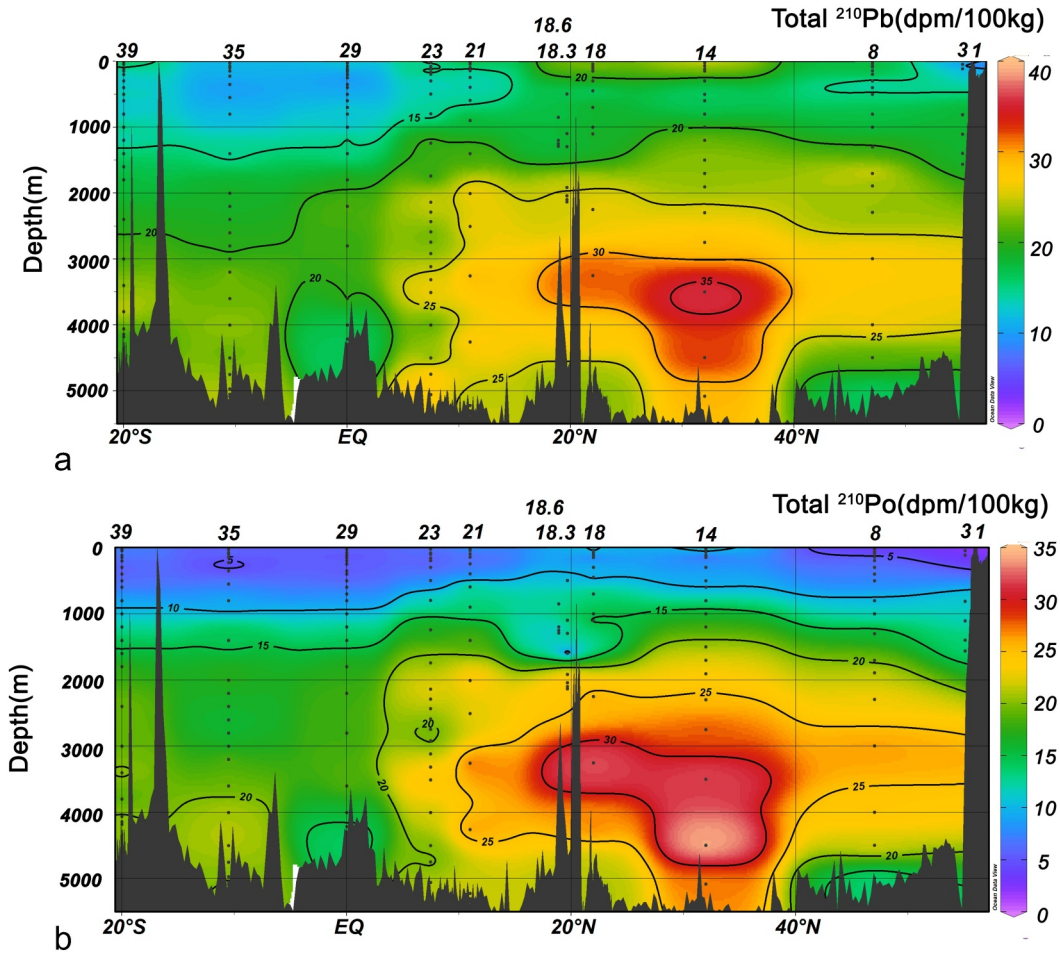

Figure 5. Total (particulate + dissolved) (a) ^{210}Pb and (b) ^{210}Po activities (dpm/100 kg) along the GP15 transect.

samples were collected by in situ pumps on different casts from the water samples. Efforts were made to match the depths of the pump and water casts, but there was often a slight offset in the former from the latter due to the wire angle. We summed the particulate fractions from the nearest depth to the dissolved fraction to calculate total activities. A significant exception occurred at station 18. The in situ pumps were turned on before reaching their target depths for samples deeper than 3,250 m and total activities were not calculated for the four deepest samples at that station.

Total ^{210}Pb activities in the upper 1,000 m increase from the lowest values on the Alaskan shelf to a maximum in the subtropical northern region around 30°N (station 14) and gradually decrease to low values in the equator and the tropical south (Figure 5a; Data Set S1). At depth, the most notable trend is the ^{210}Pb activity maximum between 3,000 and 4,000 m at station 14 (32°N), with elevated activities extending from station 14 into the surrounding water. It is also evident that lower activities are observed in the near-bottom nepheloid layers, especially near 50°N and the equator.

Total ^{210}Po activities generally increase with depth (Figure 5b), albeit with a decrease in near-bottom nepheloid layers as described for total ^{210}Pb. The source of ^{210}Po in the oceans is decay of its grandparent ^{210}Pb, and the ^{210}Po/^{210}Pb activity ratio shows that scavenging of ^{210}Po is pronounced in the upper water column (^{210}Po/^{210}Pb < 1–~1,000 m), below which the two radionuclides are close to radioactive equilibrium (^{210}Po/^{210}Pb = 1; Figure 6, Data Set S1).

The total ^{210}Pb/^{226}Ra activity ratio shows excesses of ^{210}Pb (^{210}Pb/^{226}Ra > 1) in the upper 400–700 m, with values decreasing toward radioactive equilibrium (^{210}Pb/^{226}Ra = 1) and then decreasing further toward the bottom (Figure 7). The GP15 section shows an extensive zone of near equilibrium ^{210}Pb/^{226}Ra from ~1,000 to

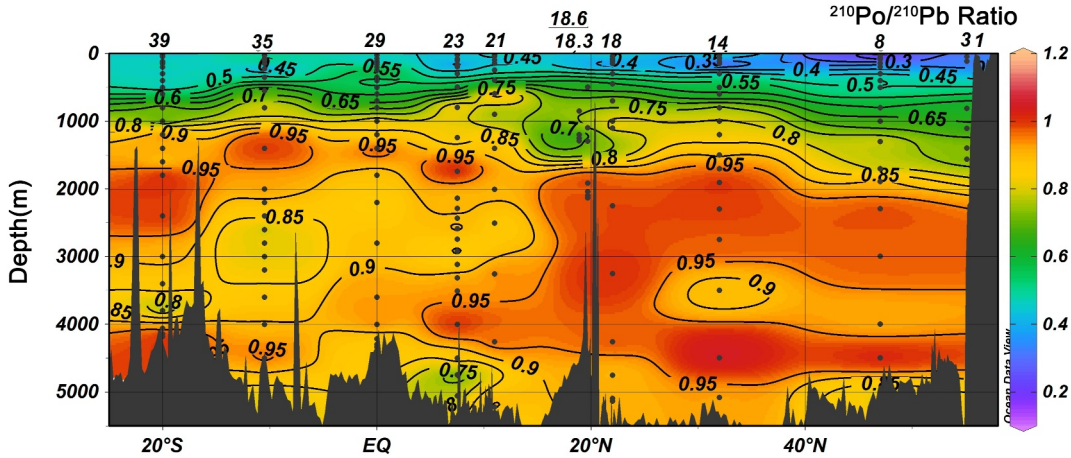

Figure 6. Section showing the activity ratio (dpm/dpm) of total ^{210}Po to total ^{210}Pb along the GP15 transect.

~4,000 m north of ~20°N, with scavenging in the bottom ~1,000 m. In contrast, south of ~7°N (stn. 23), there is an extensive zone of ^{210}Pb/^{226}Ra < 1 centered on the equator (Figure 7). Net removal of total ^{210}Pb by uptake onto particles and particle sinking is indicated by ^{210}Pb$_{total}$/^{226}Ra activity ratios <1. Removal of ^{210}Pb in the upper water column where ^{210}Pb$_{total}$/^{226}Ra is greater than 1 is also occurring but requires mass balance calculations to resolve (Section 4.1).

4. Discussion

4.1. Patterns and Rates of Scavenging of ^{210}Po and ^{210}Pb

In the simplest conception, scavenging of ^{210}Po and ^{210}Pb proceeds through their association with particles after their production from their parents (and introduction from the atmosphere to the surface water in the case of ^{210}Pb) and the removal of the particles from the water column to create a deficit of the daughter radionuclide relative to supply. Considering the total ^{210}Pb activities, the relationship between ^{210}Pb and its grandparent ^{226}Ra is shown in Figures 7 and 8.

Excesses of ^{210}Pb (^{210}Pb/^{226}Ra > 1) are evident in the surface water at all stations, with particularly high ^{210}Pb/^{226}Ra activity ratios observed at stations 14 and 18 between ~20° and 40°N (Figures 7 and 8). These high ^{210}Pb/^{226}Ra ratios are due to the input of ^{210}Pb to the surface ocean from the atmosphere (Turekian et al., 1977; Z. Wei et al., 2022). Along the GP15 transect, the atmospheric ^{210}Pb flux is highest in the North Pacific region,

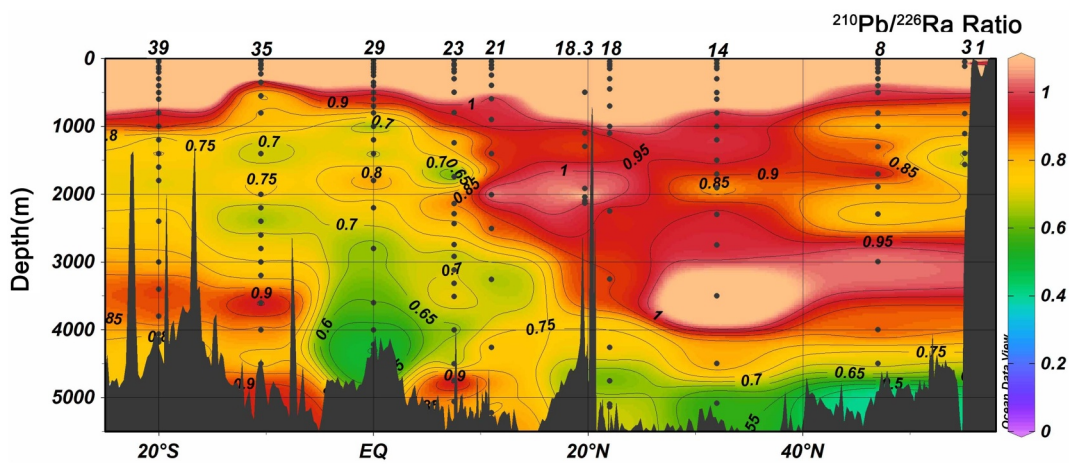

Figure 7. Section showing the ratio of total ^{210}Pb activity to ^{226}Ra activity (dpm/dpm) along the GP15 transect.

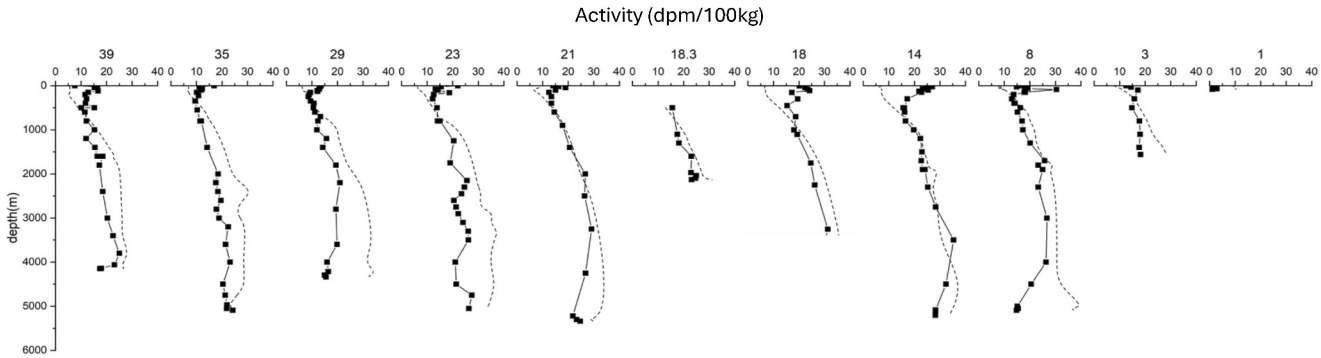

Figure 8. Profiles of total ^{210}Pb activity (filled circles; dpm/100 kg) versus depth along the GP15 transect. Dashed lines are ^{226}Ra (dpm/100 kg) profiles.

largely owing to transport from Asia (Cochran & Kadko, 2022a, 2022b; Z. Wei et al., 2022), although all stations along the transect show the influence of atmospheric deposition of ^{210}Pb on surface waters (Figure 8).

The transect shows several distinct patterns of variation in the $^{210}Pb_{total}/^{226}$Ra activity ratio with depth (Figure 7). The northernmost stations (3 and 8) show ratios <1 from ~500 to 2,500 m, possibly related to boundary scavenging on the Alaskan margin and consistent with the very low $^{210}Pb_{total}/^{226}$Ra ratios at stn. 1 (Data Set S1). Stations from ~11° to 40°N display near-equilibrium ratios from ~1,000 to 4,000 m, with pronounced low values (<0.75) deeper than ~4,500 m, corresponding to scavenging and particle export in the nepheloid layer. South of 11°N (stns. 23 to 39), there is a pronounced zone of ^{210}Pb/^{226}Ra < 1 deeper than ~1,000 m. The pattern is especially evident in association with a "particle veil" at the equator (stn. 29) and East Pacific Rise (EPR) emissions at stn. 35. These low ratios coincide with maxima in non-lithogenic particulate manganese (Chmiel et al., 2022; see also Figure S5 in Supporting Information S1) and suggest ^{210}Pb scavenging and particle export associated with Mn-enriched particles.

In contrast to the ^{210}Pb/^{226}Ra pattern, the ^{210}Po/^{210}Pb activity ratio is less than equilibrium in the upper 1,000–1,500 m at all stations, primarily reflecting scavenging (Figure 6). Aerosol data from GP15 (Z. Wei et al., 2022) show that virtually no ^{210}Po is deposited from the atmosphere, consistent with the relatively short residence times of aerosols. This may contribute to the ^{210}Po deficit in the upper water column, but the longer residence time of ^{210}Pb with respect to scavenging removal buffers any ^{210}Po deficit arising from direct aerosol deposition as discussed below. At depth, the two radionuclides are close to equilibrium, especially in the northern part of the transect. Exceptions include ^{210}Po/^{210}Pb activity ratios significantly less than 1 in samples associated with the EPR (~2,500 m; station 35), and near the bottom at the equatorial stations 29 and 23.

We can quantify these scavenging patterns using simple models of the processes (i.e., first-order scavenging) governing ^{210}Pb and ^{210}Po. For ^{210}Pb:

$$\frac{\partial A_{Pb}}{\partial t} = A_{Ra}\lambda_{Pb} - A_{Pb}\lambda_{Pb} + I_{Pb} - k_{Pb}A_{Pb} \pm V \quad (1)$$

where A_{Pb} is the total ^{210}Pb activity (dpm/m^3), A_{Ra} is the ^{226}Ra activity (dpm/m^3), I_{Pb} is the flux of ^{210}Pb from the atmosphere to the surface ocean (dpm/m^3/y), k_{Pb} is the first-order scavenging rate constant for Pb (1/y), λ_{Pb} is the decay constant for ^{210}Pb (y^{-1}), and V corresponds to vertical and horizontal advective fluxes of ^{210}Pb (dpm/m^3/y). Here, k represents the combined effects of uptake onto particles and removal of particles from the water column.

A similar model can be applied to the distribution of ^{210}Po:

$$\frac{\partial A_{Po}}{\partial t} = A_{Pb}\lambda_{Po} - A_{Po}\lambda_{Po} - k_{Po}A_{Po} \pm V \quad (2)$$

where A_{Po} is the total ^{210}Po activity and the other terms are as in Equation 1, but for ^{210}Po. Equation 2 assumes no input of ^{210}Po from the atmosphere. Z. Wei et al. (2022) found that essentially to be the case along the GP15 transect; the ^{210}Po/^{210}Pb activity ratios in aerosols collected along the transect were zero within the uncertainty.

We do not include a remineralization term for ^{210}Po in Equation 2 because the focus is on the PPZ, and the scavenging term ($k_{Po}A_{Po}$) represents the net removal of ^{210}Po due to Po uptake on particles and particle sinking. Net remineralization is likely to be more important below the PPZ where it may exceed scavenging removal in magnitude.

We approach the determination of Po and Pb residence times through the calculation of fluxes in two critical zones: the primary production zone (PPZ; Kenyon, 2022) and water deeper than 4,000 m, essentially the nepheloid layer. We make two simplifications to Equations 1 and 2. First, we assume a steady state such that $\partial A/\partial t = 0$. It is difficult to check this assumption, although a comparison of our ^{210}Pb data at station 14 with that at GEOSECS station 212 (Figure S1 in Supporting Information S1) shows remarkable similarity in profiles over a period of 45 years. One term in Equation 1 that can change seasonally is the atmospheric input of ^{210}Pb (I_{Pb}). In part, this was evaluated by Z. Wei et al. (2022), who compared the GP15 ^{210}Pb fluxes with previous measurements at comparable stations from 20°N to 10°S. Agreement was quite good with the GP16 results (2013; Niedermiller & Baskaran, 2019) and with SEAREX data from atmospheric collections at island sites in the 1970s (Turekian et al., 1989). Variability in Asian dust inputs may affect the mid-latitude atmospheric ^{210}Pb flux. Maximum inputs of Asian dust in the spring (Buck et al., 2013) were higher than the dust inputs measured on GP15 (Marsay et al., 2022). This effect would be greatest on GP15 at station 8 (47°N), which had the highest measured ^{210}Pb flux along the transect (Z. Wei et al., 2022). However, aerosol collections near 47°N on the GP15 transect produced ^{210}Pb concentrations (0.016–0.025 dpm/m$^3_{air}$; Z. Wei et al., 2022) that were comparable to those measured at Midway Island during the SEAREX program (~0.017 dpm/m$^3_{air}$; Turekian et al., 1989). Thus, we use the ^{210}Pb fluxes measured on GP15 in Equations 1 and 3 (Z. Wei et al., 2022).

We also assume that the vertical and horizontal advective terms in Equations 1 and 2 are generally negligible compared with the other terms. A similar assumption was made by Kenyon (2022) in her interpretation of ^{234}Th data from the GP15 transect, and we evaluate it below with respect to the equatorial station 29. Kenyon (2022) used the PPZ instead of the euphotic zone to consider export from the upper water column because photosynthetically active radiation data that would help define the euphotic zone were not collected on GP15. Instead, Kenyon (2022) used the depth at which fluorescence attained 10% of its maximum value, as defined by Owens et al. (2015) and Buesseler, Boyd, et al. (2020). PPZ depths ranged from ~70 to ~250 m over the transect, with most stations ~150 m (Kenyon, 2022; Table 1). In the zones of interest, we used trapezoidal integration to obtain the respective ^{210}Pb and ^{210}Po deficits and rearranged Equations 1 and 2 to yield the fluxes due to scavenging (=$k\int A_{Pb}$; J_{Pb}, $J_{Po;}$ dpm/m^2/y).

Thus, for ^{210}Pb in the PPZ,

$$J_{Pb} = \lambda_{Pb} \int (A_{Ra} - A_{Pb})\, dz + I_{Pb\text{-}} \tag{3}$$

and in deeper depths, including the nepheloid layer,

$$J_{Pb} = \lambda_{Pb} \int (A_{Ra} - A_{Pb})\, dz \tag{4}$$

For ^{210}Po, we emphasize its scavenging in the PPZ because the activity ratios of ^{210}Po/^{210}Pb are close to equilibrium in the deep water:

$$J_{Po} = \lambda_{Po} \int (A_{Pb} - A_{Po})\, dz \tag{5}$$

In general, information is lacking to fully consider the horizontal and vertical advective transport terms in Equations 1 and 2. Vertical advection via upwelling is well documented at the equator, and we attempted to account for that in the ^{210}Po and ^{210}Pb fluxes at the equatorial station (stn. 29) using the approaches of Tang et al. (2019) and Kenyon (2022). Tang et al. (2019) calculated upwelling fluxes as

$$F_w = w_{20} \times \left(A^2_{Po,Pb} - A^1_{Po,Pb}\right) \tag{6}$$

10.1029/2024GB008243

Table 1
Fluxes and Residence Times

Station	Latitude[a]	Depth of PPZ (m)[b]	Integration depth (m)	Σ^{226}Ra (10^4 dpm/m^2)	Σ^{210}Pb (10^4 dpm/m^2)	Σ^{210}Po (10^4 dpm/m^2)	I_{210Pb}[c] (dpm/m^2/d)	J_{210Pb} (dpm/m^2/d)	J_{210Po} (dpm/m^2/d)	Residence time Pb (y)	k_{Pb} (y^{-1})	Residence time Po (y)	k_{Po} (y^{-1})
Particle Production Zone (PPZ)													
3	55	77	100	1.07 ± 0.02	1.59 ± 0.08	0.46 ± 0.03	5.0 ± 3.1	4.5 ± 3.1	56.7 ± 4.3	9.6 ± 6.5	0.10 ± 0.07	0.22 ± 0.02	4.5 ± 0.5
8	47	69	65	0.55 ± 0.01	1.21 ± 0.04	0.40 ± 0.01	42.4 ± 11.2	41.8 ± 11.2	40.8 ± 2.2	0.8 ± 0.2	1.26 ± 0.34	0.27 ± 0.02	3.7 ± 0.2
14	32	167	150	1.04 ± 0.01	3.81 ± 0.12	1.57 ± 0.03	13.7 ± 6.4	11.3 ± 6.5	112 ± 6.4	9.2 ± 5.3	0.11 ± 0.06	0.38 ± 0.02	2.6 ± 0.1
18	22	181	150	0.85 ± 0.03	3.41 ± 0.12	1.52 ± 0.03	13.7 ± 6.4	11.5 ± 6.4	94.9 ± 6.1	8.1 ± 4.5	0.12 ± 0.07	0.44 ± 0.03	2.3 ± 0.2
21	11	149	145	1.04 ± 0.02	2.44 ± 0.10	1.04 ± 0.03	13.7 ± 6.4	12.5 ± 6.4	70.1 ± 5.2	5.3 ± 2.7	0.19 ± 0.10	0.41 ± 0.03	2.4 ± 0.2
23	7.5	167	160	1.08 ± 0.02	2.61 ± 0.07	1.03 ± 0.02	13.7 ± 6.4	12.4 ± 6.4	79.1 ± 3.6	5.8 ± 3.0	0.17 ± 0.09	0.36 ± 0.02	2.8 ± 0.2
29	0	115	115	0.75 ± 0.02	1.54 ± 0.07	0.73 ± 0.02	7.1 ± 2.2	6.4 ± 2.2	40.6 ± 3.6	6.6 ± 2.3	0.15 ± 0.05	0.49 ± 0.05	2.0 ± 0.2
35	−10.5	173	150	1.03 ± 0.02	1.86 ± 0.05	0.90 ± 0.02	7.1 ± 2.2	6.4 ± 2.2	48.1 ± 2.6	8.0 ± 2.8	0.13 ± 0.04	0.51 ± 0.03	2.0 ± 0.1
39	−20	240	200	1.12 ± 0.05	2.97 ± 0.15	1.43 ± 0.03	7.1 ± 2.2	5.5 ± 2.2	76.8 ± 7.6	14.7 ± 5.9	0.07 ± 0.03	0.50 ± 0.05	2.0 ± 0.2
>4,000 m		Bottom depth (m)	Integration interval (m)										
8	47	5,125	4,000–5,000	33.23 ± 0.60	22.12 ± 0.95	21.13 ± 0.68	–	9.5 ± 0.7	50 ± 57	63 ± 5	0.016 ± 0.001	12 ± 13	0.09 ± 0.10	49.8	63			0
14[d]	32	5,263	–	–	–	–	–	–	–	–	–	–	–					
18[e]	22	5,205	–	–	–	–	–	–	–	–	–	–	–	–	–			–
21	11	5,386	4,250–5,340	36.70	28.27 ± 1.27	27.06 ± 0.75	–	7.2 ± 0.9	60 ± 74	108 ± 14	0.009 ± 0.001	13 ± 15	0.08 ± 0.10				15.3	
23	7.5	5,232	4,002–5,055	37.20 ± 0.47	26.30 ± 1.05	19.38 ± 0.47	–	9.3 ± 0.3	347 ± 58	78 ± 4	0.013 ± 0.001	1.5 ± 0.3	0.67 ± 0.13	347			0	
29	0	4,380	4,000–4,335	11.05 ± 0.26	5.75 ± 0.25	4.85 ± 0.13	–	4.5 ± 0.2	45 ± 14	35 ± 2	0.029 ± 0.002	2.9 ± 0.9	0.34 ± 0.11		2			
35	−10.5	5,146	4,500–5,090	29.37 ± 0.59	25.49 ± 0.90	23.34 ± 0.48	–	3.3 ± 0.4	108 ± 51	207 ± 27	0.005 ± 0.001	5.9 ± 2.8	0.17 ± 0.08			0.00	0.001	
39[f]	−20	4,301	4,060–4,180	3.18 ± 0.07	2.56 ± 0.12	2.52 ± 0.10	–	0.5 ± 0.1	2 ± 8	132 ± 25	0.008 ± 0.001	33 ± 120	0.03 ± 0.11	2				

[a]Negative values are south. [b]From Kenyon (2022). [c]Regional average atmospheric ^{210}Pb flux (Z. Wei et al., 2022). [d]Insufficient data resolution >4,000 m. [e]No total activities >3,200 m. [f]Restricted integration depth (120 m).

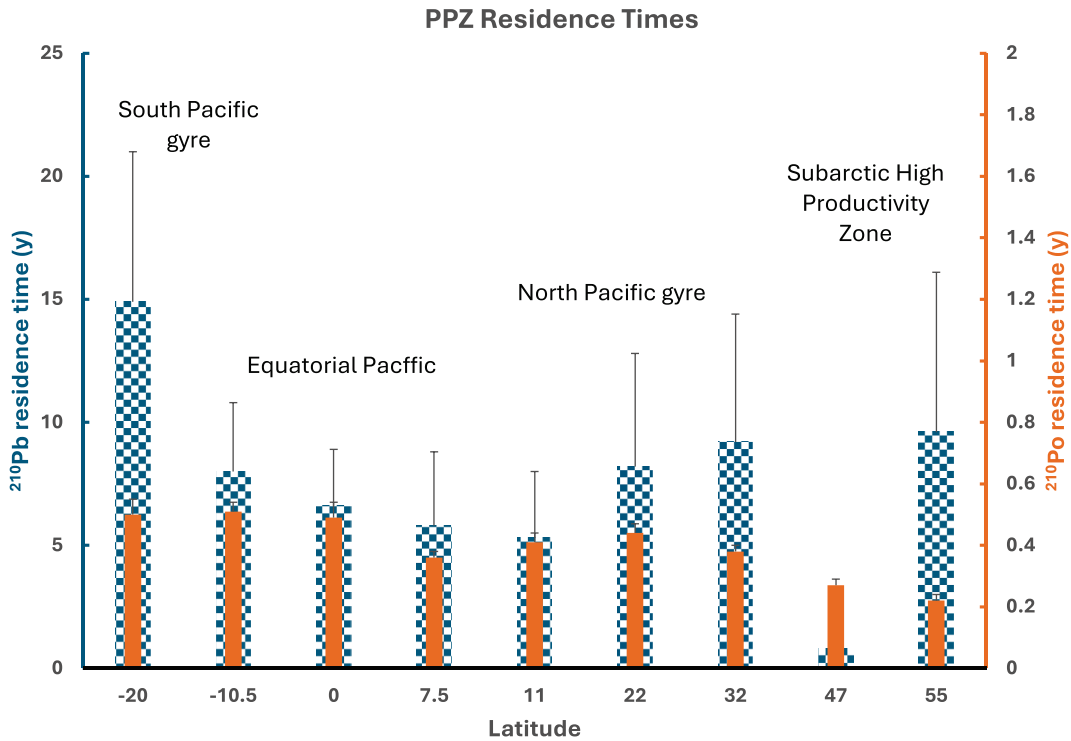

Figure 9. Residence times (y) of total ^{210}Pb (hatched blue) and total ^{210}Po (orange) with respect to scavenging in the primary production zone at the stations sampled, plotted as a function of station latitude along 152°W. Negative latitudes are south.

where F_w is the upwelling flux of ^{210}Po or ^{210}Pb (dpm/m^2/d), w_{20} is the rate of upwelling into the PPZ (m/d), $A^2_{\text{Po, Pb}}$ is the activity at a depth 20 m below the PPZ and $A^1_{\text{Po, Pb}}$ is the average activity in the PPZ (dpm m^{-3}). However, the difference in activities in each case is negative, with large propagated errors (∼100%). Negative fluxes are hard to account for and belie the documented deficiencies of both ^{210}Po (relative to ^{210}Pb) and ^{210}Pb (relative to ^{226}Ra and atmospheric supply) in the PPZ. Accordingly, we did not include them in the calculation of export fluxes in Table 1.

The formulation of ^{210}Pb and ^{210}Po fluxes as in Equations 3–5 lends itself to two calculations. First, the residence time, τ (=1/k), of ^{210}Pb or ^{210}Po with respect to scavenging in the regions of interest can be expressed as Equation 7, the quotient of the standing crop of ^{210}Pb or ^{210}Po in the zone (dpm/m^2) and the respective fluxes out due to scavenging (dpm/m^2/y):

$$\tau_{\text{Pb,Po}} = \frac{\int A_{\text{Pb,Po}}}{J_{\text{Pb,Po}}} \quad (7)$$

Second, the fluxes of ^{210}Pb and ^{210}Po (J_{Pb}, J_{Po}) from the PPZ can be used to calculate the export flux of POC from this zone, as discussed in Section 4.2.

The residence times of ^{210}Po with respect to scavenging in the PPZ are shorter than those of ^{210}Pb at all stations, reflecting the more particle-reactive nature of polonium, especially in this zone of biogenic particle production. In addition, the residence times show trends linked to the oceanographic regimes crossed in the GP15 transect (Table 1; Figure 9). Residence times for ^{210}Pb (Figure 9) are shortest at the high productivity subarctic station at 47°N (stn. 8: 0.8 y for ^{210}Pb), increase to ∼8–9 y in the North Pacific gyre then decrease toward the equator (∼5–7 y) and increase into the oligotrophic South Pacific (8–15 y). ^{210}Po shows a similar trend (Figure 9) with values ranging, from 0.2 to 0.3 y in the subarctic North Pacific to ∼0.5 y in the South Pacific (Table 1).

We note that lower atmospheric fluxes of ^{210}Pb applied to Equation 3 would produce longer residence times of ^{210}Pb with respect to scavenging. Similarly, anomalously low ^{210}Po activities in the PPZ related to the methodological artifact described in Section 2.5 would produce higher calculated ^{210}Po fluxes in Equation 5 and

consequently shorter residence times of ^{210}Po. Nevertheless, the residence times determined from the GP15 ^{210}Po and ^{210}Pb data generally agree with those from previous studies which also showed residence times of ^{210}Po shorter than ^{210}Pb. For example, Nozaki et al. (1976) calculated 1.7 y for ^{210}Pb and 0.82 y for ^{210}Po for North Pacific stations that included the GP15 transect stations.

Niedermiller and Baskaran (2019) calculated residence times of ^{210}Pb ranging from 6.8 to 195 years in the upper 300 m along the GP16 East Pacific transect. Residence times of ^{210}Po ranged from 1.9 to 8.3 years. At the crossover station occupied on both cruises, the residence time for ^{210}Pb was 45 ± 2 y on GP16 and 8.0 ± 2.8 y on GP15. Comparable values for ^{210}Po were 8.3 ± 5 y (GP16) and 0.5 ± 0.3 y (GP15). Explanations for the differences include the different timing of the cruises, integration to <200 m for most stations on GP15 versus 300 m for GP16, and different values for the atmospheric flux (lower on GP16) used to calculate the residence time of ^{210}Pb. Residence times for ^{210}Pb in the bottom 300 m ranged from 18 to 400 y on GP16 and 33 to 158 y (4,000 m to the bottom) on GP15 (Table 1). Cochran et al. (1990) calculated whole water column residence times of 27–260 y for ^{210}Pb in the Pacific but did not calculate separate values for the upper water column and near-bottom nepheloid layer.

More detailed scavenging models than the one applied above consider multiple particle size-classes (e.g., small, large particles), reversible scavenging between solution and particles, particle-particle interactions (e.g., aggregation, disaggregation) and large particle settling (see Cochran & Masqué, 2003 for a summary). Rigaud et al. (2015) applied a reversible scavenging model to ^{210}Po and ^{210}Pb data from the GEOTRACES North Atlantic GA03 section. Such a model allows for calculation of the residence times of dissolved Po or Pb relative to scavenging onto small particles and particulate Po and Pb residence times relative to net aggregation of small to large particles and net removal of large particles via sinking. The dissolved residence times in the model used by Rigaud et al. (2015) most approximate those calculated using the simple scavenging model above. Rigaud et al. (2015) found that the dissolved residence times for ^{210}Po in the surface ocean ranged from 0.07 to 0.53 y and those for ^{210}Pb ranged from 3 to 6 y. These values are generally comparable with those from the GP15 transect (Figure 9; Table 1).

A consequence of reversible scavenging is that it permits a sorption equilibrium of radionuclide to be attained between particles and solution. Indeed, evidence for the reversible scavenging of particle-reactive radionuclides through the water column was first demonstrated for ^{230}Th by Bacon and Anderson (1982). They observed that both particulate and dissolved ^{230}Th increased with depth in the water column, a situation that could only be caused by reversible scavenging. Using stable Pb isotope data from the GP15 transect, Lanning et al. (2023) invoked reversible scavenging to explain the penetration of anthropogenic stable Pb isotope ratios of dissolved Pb deeper in the water column than would be possible from abyssal mixing alone. They argued that the effect was especially evident at stations corresponding to high particulate inorganic carbon (and suspended particulate matter, SPM) denoted as "particle veils," notably stations 10–12 and at the equator, station 29.

Our data also show evidence of reversible scavenging of both ^{210}Po and ^{210}Pb. The dissolved concentrations of both radionuclides increase with depth in the water column, largely driven by the production of ^{210}Pb from ^{226}Ra (e.g., Figures 3a and 3b). Particulate activities also increase. Table 2 shows that the average middepth (~500–3,500 m) activity ratios of particulate-to-dissolved radionuclide are rather constant. We use the small particle activities in this calculation because they likely have higher surface areas for radionuclide adsorption and are less affected by artifacts of particle breakthrough that may have affected the large particle fraction. Sorption artifacts on the small particle fraction should introduce only ~10% overestimate of the small particle activities for ^{210}Po and ^{210}Pb (see Section 3.1.2). Ratios of small particle-to-dissolved activity for ^{210}Pb range from 0.005 ± 0.002 to 0.017 ± 0.005 for stations north of the equatorial station 29; comparable values for ^{210}Po range from 0.059 ± 0.018 to 0.097 ± 0.009 (Table 2). We exclude stations north of station 8 (i.e., 1 and 3) from the tabulation because they are shelf and slope stations. Particulate-to-dissolved ratios are higher for both radionuclides at stations south of the equator (stns. 35 and 39; Table 2).

These ratios can be converted to distribution coefficients (Kd; mL/g) by dividing by the average small particle concentration over the same depths. The Kd values are ~10^7 for ^{210}Po and ~10^6 for ^{210}Pb, consistent with the greater particle reactivity of Po compared with Pb. Both radionuclides show higher Kd values in the South Pacific. These track the lower particle concentrations at those stations than the equator and North Pacific stations (Table 2). The Kd values are similar to those determined in laboratory Kd measurements of ^{210}Po and ^{210}Pb (e.g., Chuang et al., 2013) and to values measured in the Pacific Ocean, as summarized by Bam et al. (2020) and Planaj

Table 2
Middepth (~500–3,500 m) Small Particle Particulate/Dissolved Activity Ratios and Kd Values

Station	$^{210}Po_{sp}/^{210}Po_d$	$^{210}Pb_{sp}/^{210}Pb_d$	Depths (m)	Avg. Sp[a] (mg/L)	Kd ^{210}Po (10^6 mL/g)	Kd ^{210}Pb (10^6 mL/g)
8	0.085 ± 0.028	0.005 ± 0.002	500–3,000	5.9	14	0.8
14	0.067 ± 0.029	0.010 ± 0.002	500–3,500	3.9	17	2.6
18	0.068 ± 0.022	0.017 ± 0.005	450–3,170	3.3	21	5.2
21	0.062 ± 0.024	0.008 ± 0.004	400–3,260	3.5	18	2.3
23	0.059 ± 0.018	0.012 ± 0.005	500–3,500	2.5	24	4.8
29	0.097 ± 0.009	0.015 ± 0.009	500–3,600	5.9	16	2.5
35	0.134 ± 0.077	0.027 ± 0.013	550–3,600	2.1	64	13
39	0.148 ± 0.028	0.025 ± 0.009	500–3,400	1.6	93	16

[a]Sp = small particle size fraction (0.8–51 μm).

and Baskaran (2024). Bam et al. (2020) showed Kd ranges from 10^7 to 10^8 for ^{210}Po and 10^6 to 10^7 for ^{210}Pb over the particle concentrations shown in Table 2 with higher values at lower particle concentrations. Bam et al. (2020) also reported higher values from samples along the GEOTRACES Arctic Transect and concluded that higher particulate Mn was at least partly responsible. Summarizing Kd values in the Pacific Ocean, Planaj and Baskaran (2024) reported values ranging from 0.5 to 5.9 × 10^6 for ^{210}Pb and 0.3–15 × 10^6 for ^{210}Po in the South China Sea over approximately the same depths as considered in Table 2. However, the particle concentrations in the South China Sea (51–400 μg/L) were higher than those for the GP15 samples.

The trend toward higher Kd with lower particle concentrations may be caused by the "particle concentration effect" (Honeyman & Santschi, 1989; Hong et al., 2008; Li et al., 1984) or by differences in particle type and composition. Considering a particle concentration effect, Honeyman and Santschi (1989) observed little change in Kd's of ^{234}Th for particle concentrations less than 100 μg/L. Similarly, Bam et al. (2020) showed relatively little change in Kd's for ^{210}Po and ^{210}Pb for small particle concentrations ranging from 1 to 3–4 μg/L, approximately the same range as the middepth concentrations along GP15. In contrast, particle type may play a larger role. For example, Lin et al. (2021) observed that Po is enriched in exopolymers derived from coccolithophores. Indeed, the small particulate fraction is enriched in $CaCO_3$ at station 39, where Kd values are high, but also broadly from 25° to 40°N, where Kd values are lower (Figure S5 in Supporting Information S1). Other aspects of particle composition are likely important. Both South Pacific stations (35 and 39) are affected by hydrothermal emissions from the EPR. This is evident in the higher particulate excess (non-lithogenic) Mn at those stations (Chmiel et al., 2022), suggesting that Mn may be an important scavenging agent for both radionuclides. Indeed, the relative minima of dissolved ^{210}Po and ^{210}Pb and maxima in particulate activities at ~2,500–3,000 m at Station 35 (Figures 3a, 3b, 4a, and 4b) are likely related to EPR emissions. A more detailed consideration of controls on particulate and dissolved ^{210}Po and ^{210}Pb along the GP15 transect is in preparation.

4.2. ^{210}Po and ^{210}Pb as Proxies for POC Export From the Photic Zone

4.2.1. POC Fluxes

An important application of the mass balances of ^{210}Po and ^{210}Pb determined above (Table 1) is their use as proxies for the sinking flux of POC from the euphotic zone. The fluxes of these radionuclides were determined using Equations 3 and 5 (i.e., J_{Pb} and J_{Po}) can be converted into the flux of POC by multiplying by the ratio of POC in sinking particles leaving the photic zone to that of particulate Pb or Po on the same particles:

$$J_{POC} = \left(\frac{POC}{P_{Pb,Po}}\right)_L \times J_{Pb,Po} \quad (8)$$

where J_{POC} is the sinking flux of POC (mmol/m^2/d), $(POC/P_{Pb,Po})_L$ is the ratio of POC to particulate ^{210}Pb or ^{210}Po on the large particle fraction (mmol/dpm) at the base of the PPZ, and $J_{Pb,\,Po}$ are the fluxes of ^{210}Pb and ^{210}Po from the PPZ (dpm/m^2/d; Equations 3 and 5; Table 3).

This approach has been widely used for other parent/daughter radionuclide pairs, especially $^{234}Th/^{238}U$ (e.g., Buesseler et al., 1992; Buesseler, Benitez-Nelson, et al., 2020; Lemaitre et al., 2018; Owens et al., 2015), as well as with other Th isotopes (Hayes et al., 2018), and with $^{210}Po/^{210}Pb$ and $^{210}Pb/^{226}Ra$ (e.g., Bam et al., 2020; Hayes et al., 2018; Horowitz et al., 2020; Stewart et al., 2007, 2010; Tang & Stewart, 2019; C.-L. Wei et al., 2017). Here we use the PPZ to approximate the photic zone. We combined particulate ^{210}Pb and ^{210}Po data at the base of the PPZ with POC data (Amaral et al., 2024) to calculate the POC/Pb_p and POC/Po_p ratios (Table 3). As noted in Section 2.2, particulate samples were collected in two size fractions– a "large" size (>51 μm) and a "small" size (0.8–51 μm)– using in situ pumps. We note that the ^{210}Po and ^{210}Pb fluxes were calculated using Equations 3 and 5 correspond to total fluxes caused by sinking of both small and large particles. Classically, data from the large size fraction are used to calculate POC fluxes (Equation 8) using radionuclide proxies because they are assumed to best represent the sinking particles and be largely responsible for the radionuclide deficits. We calculate POC fluxes and compare the values calculated with both particle size fractions, with the caveat that the true POC flux likely lies between the estimates, with a bias toward the values derived from the large particle data.

There is considerable variation in the POC flux along the GP15 transect (Table 3; Figure 10).

The ^{210}Po-derived POC flux is consistently greater than that from the ^{210}Pb balance. POC fluxes derived using the ^{210}Po deficit relative to ^{210}Pb and the $POC/^{210}Po$ on the large particle fraction range from 15.5 ± 1.3 to 1.5 ± 0.2 mmol m^{-2} d^{-1} and those calculated using the ^{210}Pb balance range from 6.7 ± 1.8 mmol m^{-2} d^{-1} to 0.2 ± 0.1 mmol m^{-2} d^{-1}.

Both proxies show highest fluxes in the northern part of the transect, especially in the high productivity Subarctic North Pacific. POC fluxes from both proxies are also relatively high near but not at the equator (station 23, 7.5°N; Figure 10). A similar regional pattern of high fluxes in the Subarctic North Pacific was seen by Kenyon (2022) in her application of $^{234}Th/^{238}U$ disequilibrium to determine POC fluxes. Diatoms and coccolithophorids dominate the particles in the subarctic section of the GP15 transect off Alaska and may be responsible for the larger POC fluxes calculated by all the radionuclide proxies there.

Fluxes calculated using the $POC/^{210}Po$ and $POC/^{210}Pb$ on the small particle fraction show similar trends along the transect but are generally lower using the ^{210}Po proxy, especially in the northern part of the transect (Table 3). POC fluxes for both the large and small particle fractions are comparable north of 22°N when calculated using ^{210}Pb, but greater using the $POC/^{210}Pb$ ratio on the small particles in the equatorial and South Pacific stations (Table 3). These patterns result from the fact that the POC/Po ratio (mmol/dpm) for the small particles is lower or comparable to that of the large particles. In contrast, the POC/Pb ratios are consistently greater for the small particles compared with the POC/Pb of the large particles. The pattern for Po fits that expected from the considerations of volume/surface area for large and small particles, assuming spherical geometry. Volume should favor POC while surface area favors surface-adsorbed radionuclides. This results in lower ratios for small particles (high surface area relative to volume). Such a trend has been documented for ^{234}Th from numerous studies (Buesseler et al., 2006), yet Kenyon (2022) observed that regional averages of the $POC/^{234}Th$ on small and large particles were essentially equal within errors along GP15.

The divergence of the patterns of $POC/^{210}Pb$ and $POC/^{234}Th$ and, to a lesser extent, $POC/^{210}Po$ from particle size considerations suggests that the simple spherical model does not apply and ignores the nature of the particles. It also emphasizes the different biogeochemical behaviors of ^{210}Po, ^{210}Pb, and ^{234}Th such that Po can be both incorporated into organic matter as well as adsorbed onto the surface, while ^{210}Pb and ^{234}Th are dominantly surface-reactive (Fisher et al., 1983).

4.2.2. Comparison of POC Fluxes Determined With ^{234}Th, ^{210}Po, and ^{210}Pb

Kenyon (2022) gives regional average values of ^{234}Th-derived POC fluxes, and we can compare these regional averages with those from ^{210}Po- and ^{210}Pb-POC flux proxies. Both the ^{210}Po- and ^{210}Pb-derived regional average POC fluxes (with large errors) display comparable trends to the ^{234}Th values but, for ^{210}Po, are consistently greater than those determined using ^{234}Th (Figure 11).

The offset of the ^{210}Pb-POC fluxes with those calculated using ^{234}Th is not as large and in fact values are quite comparable in the oligotrophic South Pacific (Figure 11). There have been few studies in the Pacific that compare ^{210}Po- and ^{234}Th-derived POC fluxes. Verdeny et al. (2009) synthesized studies comparing the fluxes at sites throughout the world ocean. Studies by Murray et al. (1996, 2005) in the central equatorial Pacific and Verdeny

10.1029/2024GB008243

Table 3
^{210}Po- and ^{210}Pb-Derived POC Fluxes- Primary Production Zone (PPZ)

Station	Latitude	Depth of PPZ (m)	Integration depth (m)	J_{210Pb} (dpm/m^2/d)	J_{210Po} (dpm/m^2/d)	POC (μmol/L)	^{210}Po (dpm/100 kg)	^{210}Pb (dpm/100 kg)	POC/^{210}Po (mmol/dpm)	POC/^{210}Pb (mmol/dpm)	Po-derived POC flux (mmol/m^2/d)	Pb-derived POC flux (mmol/m^2/d)
Large particles												
3	55	77	100	4.5 ± 3.1	56.7 ± 4.3	0.061 ± 0.001	0.040 ± 0.007	0.073 ± 0.012	0.148 ± 0.025	0.081 ± 0.014	8.4 ± 1.5	0.4 ± 0.3
8	47	69	65	41.8 ± 11.2	40.8 ± 2.2	0.657 ± 0.001	0.169 ± 0.010	0.403 ± 0.020	0.379 ± 0.023	0.159 ± 0.008	15.5 ± 1.3	6.7 ± 1.8
14	32	167	150	11.3 ± 6.5	112 ± 6.4	0.071 ± 0.001	0.094 ± 0.009	0.040 ± 0.008	0.074 ± 0.008	0.172 ± 0.034	8.3 ± 1.0	2.0 ± 1.2
18	22	181	150	11.5 ± 6.4	94.9 ± 6.1	0.047 ± 0.001	0.144 ± 0.013	0.226 ± 0.015	0.032 ± 0.003	0.020 ± 0.001	3.0 ± 0.4	0.2 ± 0.1
21	11	149	145	12.5 ± 6.4	70.1 ± 5.2	0.017 ± 0.001	0.076 ± 0.008	0.017 ± 0.005	0.022 ± 0.003	0.098 ± 0.032	1.5 ± 0.2	1.2 ± 0.8
23	7.5	167	160	12.4 ± 6.4	79.1 ± 3.6	0.030 ± 0.001	0.047 ± 0.007	0.015 ± 0.005	0.061 ± 0.009	0.186 ± 0.059	4.9 ± 0.7	2.3 ± 1.4
29	0	115	115	6.4 ± 2.2	40.6 ± 3.6	0.075 ± 0.001	0.129 ± 0.011	0.038 ± 0.008	0.057 ± 0.005	0.195 ± 0.041	2.3 ± 0.3	1.3 ± 0.5
35	−10.5	173	150	6.4 ± 2.2	48.1 ± 2.6	0.050 ± 0.001	0.117 ± 0.010	0.029 ± 0.006	0.042 ± 0.004	0.172 ± 0.042	2.0 ± 0.2	1.1 ± 0.5
39	−20	240	200	5.5 ± 2.2	76.8 ± 7.6	0.030 ± 0.001	0.052 ± 0.007	0.037 ± 0.007	0.056 ± 0.008	0.080 ± 0.015	4.3 ± 0.8	0.4 ± 0.2
Small particles												
3	55	77	100	4.5 ± 3.1	56.7 ± 4.3	0.557 ± 0.016	0.907 ± 0.058	0.490 ± 0.039	0.060 ± 0.004	0.111 ± 0.009	3.4 ± 2.4	0.5 ± 0.3
8	47	69	65	41.8 ± 11.2	40.8 ± 2.2	0.864 ± 0.015	0.676 ± 0.045	0.473 ± 0.042	0.125 ± 0.009	0.178 ± 0.016	5.1 ± 0.4	7.5 ± 2.1
14	32	167	150	11.3 ± 6.5	112 ± 6.4	0.240 ± 0.013	0.637 ± 0.044	0.111 ± 0.017	0.037 ± 0.003	0.210 ± 0.034	4.1 ± 0.4	2.4 ± 1.4
18	22	181	150	11.5 ± 6.4	94.9 ± 6.1	0.305 ± 0.012	0.853 ± 0.056	0.813 ± 0.054	0.035 ± 0.003	0.037 ± 0.003	3.3 ± 0.3	0.4 ± 0.2
21	11	149	145	12.5 ± 6.4	70.1 ± 5.2	0.172 ± 0.012	0.563 ± 0.039	0.024 ± 0.010	0.030 ± 0.003	0.689 ± 0.279	2.1 ± 0.3	8.6 ± 3.5
23	7.5	167	160	12.4 ± 6.4	79.1 ± 3.6	0.195 ± 0.013	0.501 ± 0.036	0.061 ± 0.011	0.038 ± 0.004	0.311 ± 0.057	3.0 ± 0.3	3.9 ± 2.1
29	0	115	115	6.4 ± 2.2	40.6 ± 3.6	0.440 ± 0.012	0.568 ± 0.043	0.140 ± 0.013	0.076 ± 0.006	0.308 ± 0.031	3.1 ± 0.4	2.0 ± 0.7
35	−10.5	173	150	6.4 ± 2.2	48.1 ± 2.6	0.309 ± 0.013	0.746 ± 0.053	0.104 ± 0.016	0.041 ± 0.003	0.290 ± 0.047	2.0 ± 0.2	1.9 ± 0.7
39	−20	240	200	5.5 ± 2.2	76.8 ± 7.6	0.247 ± 0.013	0.556 ± 0.053	0.141 ± 0.016	0.043 ± 0.005	0.171 ± 0.021	3.3 ± 0.5	0.9 ± 0.4

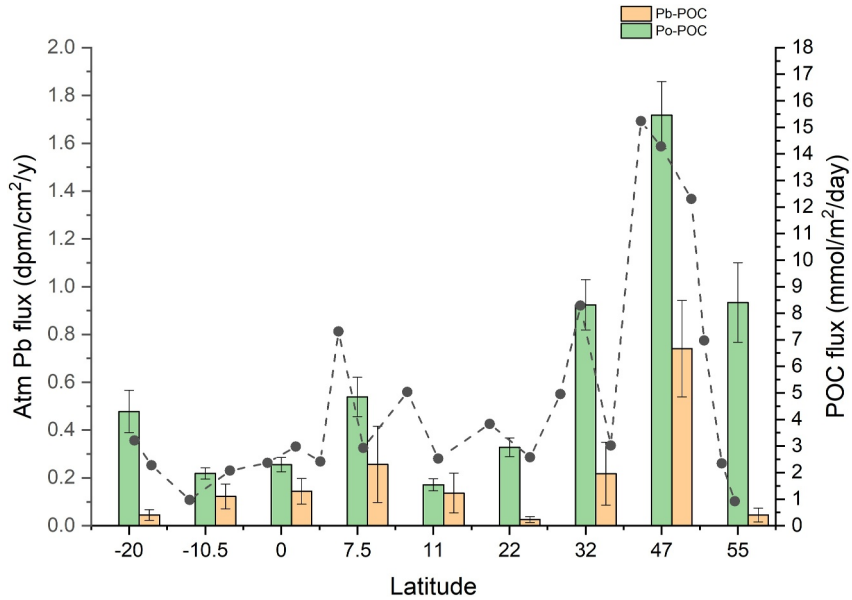

Figure 10. Particulate organic carbon fluxes from the primary production zone on particles >51 μm (mmol/m^2/d) derived from ^{210}Po (green) and ^{210}Pb (orange) balances, plotted as a function of station latitude. Negative latitudes are south. Solid black circles represent the atmospheric flux of ^{210}Pb determined in aerosol samples collected on the cruise (Z. Wei et al., 2022).

et al. (2008) in the Pacific near Hawaii show that ^{210}Po-derived POC fluxes are greater by a factor of ~2 than those derived using ^{234}Th, although this offset is not systematic elsewhere in the world ocean (e.g., Verdeny et al., 2009).

There are several possible reasons for differences in POC fluxes calculated using the various radionuclide proxies:

1. The different half-lives of the three radionuclides suggest that they integrate flux events on different time scales according to time scales given by half-life and scavenging mean residence times (i.e., $1/(\lambda + k)$). ^{234}Th with a radioactive mean-life of 35 days and rapid scavenging integrates over the prior months of sampling, while ^{210}Po (2.6 y mean life; 0.4 y scavenging mean residence time) integrates over the prior year. In contrast, ^{210}Pb (32 y mean life; ~5 y scavenging mean residence time) integrates over years. Sampling along GP15 was conducted during the boreal autumn (October-November) and a high flux event linked to a phytoplankton bloom earlier in the year might have been better recorded by ^{210}Po than ^{234}Th. Similarly, ^{210}Pb would integrate over multiple years of such events, potentially producing values intermediate between those of the ^{210}Po and ^{234}Th proxies.
2. A well-recognized problem is applying radionuclide proxies to determine POC fluxes using Equation 8 is the assumption that the measured POC/radionuclide ratio is characteristic of the exported particles that produced the deficit of the daughter relative to the parent radionuclide and thus the flux ($J_{Pb,Po,Th}$ in Equation 8: Buesseler et al., 2006). It is unclear how this might produce differences among different radionuclides applied to the POC flux. The POC/radionuclide ratio on particles remaining in the water column well after a bloom might have lost POC through remineralization. This could lower the POC/radionuclide ratio and seems to apply to POC/Pb and POC/Th as the radionuclides could remain associated with the degraded particle. In contrast, the POC/Po ratio might be 'buffered' from such changes if both POC and ^{210}Po are lost during degradation. Such differences could produce lower POC fluxes derived from ^{210}Pb or ^{234}Th than ^{210}Po. In reality, the dynamics of marine particles are complicated, with exchanges through aggregation and disaggregation occurring between the "small" and "large" particle fractions (Amaral et al., 2024; Murnane et al., 1996), and these dynamics make it difficult to predict the effects on the POC/radionuclide ratios.
3. Methodological issues may have affected the calculation of the ^{210}Po deficits. As noted in Section 2.1, ingrowth corrections were minimized by processing samples rapidly on board from extraction of ^{210}Pb and ^{210}Po from the water sample by precipitation of iron hydroxide to the initial separation of ^{210}Po from ^{210}Pb. Roca-Martí et al. (2021) observed that this approach can produce lower ^{210}Po values compared with another established

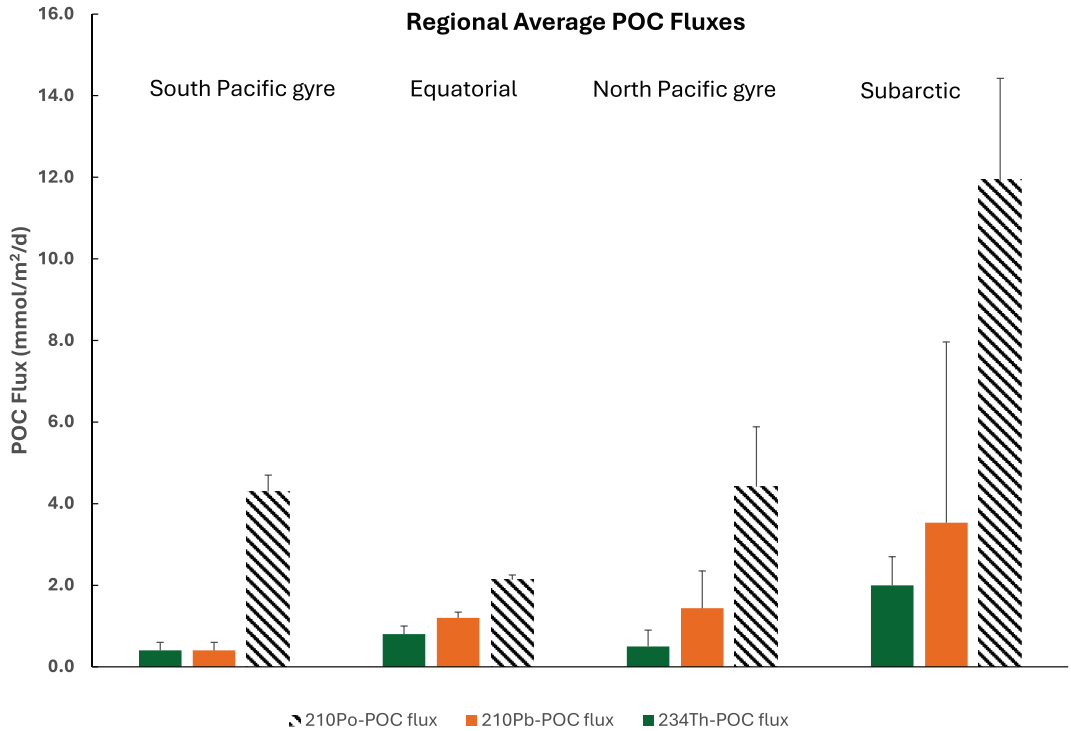

Figure 11. Comparison of regional average particulate organic carbon fluxes on particles >51 μm from the primary production zone calculated using ^{210}Po (hatched), ^{210}Pb (orange) and ^{234}Th (green; Kenyon, 2022). Regional averages follow those used for ^{234}Th in Kenyon (2022) and for ^{210}Po and ^{210}Pb comprise stations: Subarctic- 3, 8; North Pacific gyre- 14, 18, 21; Equatorial- 23, 29, 35; South Pacific gyre- 39.

method for concentrating ^{210}Po and ^{210}Pb from seawater (Co-APDC; Boyle & Edmond, 1975; Fleer & Bacon, 1984). The hypothesis underlying this observation is that a fraction of ^{210}Po is complexed with organic ligands because it has passed through the marine microbial food web (Fisher et al., 1983; Stewart et al., 2005). Such complexation may prevent some ^{210}Po from being scavenged onto the freshly precipitated iron hydroxide, but both complexed and uncomplexed forms are included in the Co-APDC aggregate. This contrasts with ^{210}Pb, which is not incorporated into organic matter, and indeed, no difference is seen in the methods when applied to ^{210}Pb (Chung et al., 1983). Recent ongoing research in the Mediterranean Sea (Cochran et al., unpublished) rigorously compares the methods and supports the results of Roca-Martí et al. (2021). A methodological artifact that yields a low ^{210}Po activity in a sample would produce an erroneously high deficit with respect to ^{210}Pb and thus a high ^{210}Po-derived POC flux. Additionally, as noted in Section 3.1.2, the large particle 51 μm filters may not have captured all the particles passing through them, as indicated by the activities of ^{210}Po and ^{210}Pb on the backing 150 μm backing filters. If this is simply produced by under-capture of bulk particles, the POC/^{210}Po and POC/^{210}Pb ratios and calculated POC fluxes would be unaffected.

For ^{210}Pb, the mass balance used to determine its flux relies on knowledge of its atmospheric flux to the PPZ (Equation 1). For most studies, this is not known, and literature values are used if the ^{210}Pb POC-flux proxy is applied at all. For GP15, atmospheric ^{210}Pb fluxes were determined in detail along the transect based on measurements of ^{210}Pb and ^{7}Be in aerosols (Z. Wei et al., 2022; Figure 10). The assumption is that the atmospheric flux is in a steady state, that is, constant with time at a given latitude (e.g., Equation 3). This assumption is rather robust for stations south of 30°N because the values determined on GP15 agree with earlier estimates from studies such as SEAREX. In the subarctic North Pacific, atmospheric ^{210}Pb fluxes were high as a consequence of air masses that originated over Siberia. Seasonal variations in air mass patterns and dust fluxes (Buck et al., 2013; Marsay et al., 2022) could cause lower ^{210}Pb fluxes, in which case the ^{210}Pb fluxes from the PPZ calculated using the GP15 values would be high.

5. Summary and Conclusions

The distributions of the natural ^{238}U-series radionuclides ^{210}Po and its grandparent ^{210}Pb along the GP15 Pacific Meridional Transect provide information on scavenging rates of reactive chemical species throughout the water column and fluxes of POC from the primary production zone, PPZ, defined as the depth at which fluorescence reaches 10% of its maximum. Measurements of activities on large (>51 μm) and small (1–51 μm) particles and in solution (<0.2 μm) show that activities are ranked as dissolved > small > large particles. Particulate ^{210}Po activities are greater than ^{210}Pb for both large and small particles, indicating its greater particle reactivity. Patterns of radioactive disequilibria provide information on the scavenging of these radionuclides. ^{210}Pb is in excess of its grandparent ^{226}Ra in the upper 400–700 m of most stations due to the atmospheric flux of ^{210}Pb. Mid-water ^{210}Pb/^{226}Ra activity ratios are close to radioactive equilibrium (^{210}Pb/^{226}Ra = 1) north of ∼20°N, but deficiencies are elevated at stations near and south of the equator. These low ratios are associated with enhanced scavenging in a "particle veil" located at the equator, possibly associated with elevated non-lithogenic particulate manganese from hydrothermal processes at the EPR. Deficiencies of ^{210}Pb relative to ^{226}Ra are also evident in the bottom 500–1,000 m at most stations due to enhanced scavenging in the nepheloid layer. The activity ratio ^{210}Po/^{210}Pb shows scavenging patterns similar to ^{210}Pb, with extensive scavenging in the PPZ and near the bottom. Residence times of ^{210}Pb with respect to scavenging in the PPZ range from 0.8 to 15y, with the lowest value in the Subarctic North Pacific and highest in the oligotrophic South Pacific. Values for ^{210}Po are lower than those for ^{210}Pb, indicating its enhanced particle reactivity and range from 0.2 to 0.5 y from the Subarctic to the South Pacific.

The deficits in ^{210}Po (relative to ^{210}Pb) and ^{210}Pb (relative to production from ^{226}Ra and addition from the atmosphere), together with POC concentrations and particulate ^{210}Po and ^{210}Pb activities, are used as proxies for calculating the sinking flux of POC from the PPZ. ^{210}Po-derived POC fluxes based on the large particle fraction range from 15.5 ± 1.3 mmol C m^{-2} d^{-1} to 2.0 ± 0.2 mmol C m^{-2} d^{-1}from Subarctic North Pacific to South Pacific; ^{210}Pb-derived fluxes range from 6.7 ± 1.8 mmol C m^{-2} d^{-1} to 0.4 ± 0.2 mmol C m^{-2} d^{-1}. A similar trend is seen in ^{234}Th-derived POC fluxes (Kenyon, 2022), although both ^{210}Po- and ^{210}Pb-derived POC fluxes are greater than those calculated using the ^{234}Th proxy. Differences among the radionuclides may be due to their different integration times considering their different radioactive mean-lives and scavenging mean residence times. Methodological issues may also play a role, especially in the Po-derived POC fluxes. Further research is needed to explore this possibility and make the application of the ^{210}Po-POC flux proxy more rigorous.

Data Availability Statement

Station-by-station ^{210}Po and ^{210}Pb data are given in Supplemental Data Set S1 and are also reposited with BCO-DMO- Dissolved: https://www.bco-dmo.org/dataset/883724; https://www.bco-dmo.org/dataset/883797; Particulate: https://www.bco-dmo.org/dataset/892348; https://www.bco-dmo.org/dataset/892360; Aerosols: https://www.bco-dmo.org/dataset/878689; https://www.bco-dmo.org/dataset/878703. ^{226}Ra data are available at: https://www.bco-dmo.org/dataset/825891 and https://www.bco-dmo.org/dataset/825947.

Acknowledgments

David Kadko was our collaborator and co-PI on this project and passed away during its final stages. He was a valued colleague and is deeply missed. We thank the crew of the R/V *Roger Revelle* for their expert shipboard operations during the GEOTRACES GP15 cruise, and Co-Chief Scientists Phoebe Lam, Karen Casciotti and Greg Cutter for their support of this project. We are grateful to the pump and rosette teams for their help in obtaining the samples used in this project. We thank two anonymous reviewers for their helpful comments. This research was supported by National Science Foundation Grants OCE-1736591 to JKC, OCE-1736319, and OCE-1736612 to MS, OCE-1736277 to MC, and OCE-1657781 and OCE-1736601 to PL.

References

Amaral, V. J., Lam, P. J., Marchal, O., & Kenyon, J. A. (2024). Cycling rates of particulate organic carbon along the GEOTRACES Pacific meridional transect GP15. *Global Biogeochemical Cycles*, *38*(1), e2023GB007940. https://doi.org/10.1029/2023GB007940

Anand, S. S., Rengarajan, R., Shenoy, D., Gauns, M., & Naqvi, S. W. A. (2018). POC export fluxes in the Arabian Sea and the Bay of Bengal: A simultaneous ^{234}Th/^{238}U and ^{210}Po/^{210}Pb study. *Marine Chemistry*, *198*, 70–87. https://doi.org/10.1016/J.MARCHEM.2017.11.005

Bacon, M. P., & Anderson, R. F. (1982). Distribution of thorium isotopes between dissolved and particulate forms in the deep sea. *Journal of Geophysical Research*, *87*(C3), 2045–2056. https://doi.org/10.1029/jc087ic03p02045

Bacon, M. P., Belastock, R. A., Tecotzky, M., Turekian, K. K., & Spencer, D. W. (1988). Lead-210 and polonium-210 in ocean water profiles of the continental shelf and slope south of New England. *Continental Shelf Research*, *8*(5–7), 841–853. https://doi.org/10.1016/0278-4343(88)90079-9

Bacon, M. P., Spencer, D. W., & Brewer, P. G. (1976). ^{210}Pb/^{226}Ra and ^{210}Po/^{210}Pb disequilibria in seawater and suspended particulate matter. *Earth and Planetary Science Letters*, *32*(2), 277–296. https://doi.org/10.1016/0012-821X(76)90068-6

Bam, W., Maiti, K., Baskaran, M., Krupp, K., Lam, P. J., & Xiang, Y. (2020). Variability in ^{210}Pb and ^{210}Po partition coefficients (Kd) along the US GEOTRACES Arctic transect. *Marine Chemistry*, *219*, 103749. https://doi.org/10.1016/J.MARCHEM.2020.103749

Boyle, E. A., & Edmond, J. M. (1975). Determination of trace metals in aqueous solution by APDC chelate co-precipitation. In *Analytical Methods in Oceanography* (pp. 44–55). American Chemical Society. https://doi.org/10.1021/ba-1975-0147.ch006

Buck, C. S., Landing, W. M., & Resing, J. (2013). Pacific Ocean aerosols: Deposition and solubility of iron, aluminum, and other trace elements. *Marine Chemistry*, *157*, 117–130. https://doi.org/10.1016/j.marchem.2013.09.005

Buesseler, K. O., Antia, A. N., Chen, M., Fowler, S. W., Gardner, W. D., Gustafsson, O., et al. (2007). An assessment of the use of sediment traps for estimating upper ocean particle fluxes. *Journal of Marine Research*, *65*(3), 345–416. https://doi.org/10.1357/002224007781567621

Buesseler, K. O., Bacon, M. P., Cochran, J. K., & Livingston, H. D. (1992). Carbon and nitrogen export during the JGOFS North Atlantic Bloom experiment estimated from ^{234}Th: ^{238}U disequilibria. *Deep-Sea Research, Part A: Oceanographic Research Papers*, *39*(7), 1115–1137. https://doi.org/10.1016/0198-0149(92)90060-7

Buesseler, K. O., Benitez-Nelson, C. R., Moran, S. B., Burd, A., Charette, M., Cochran, J. K., et al. (2006). An assessment of particulate organic carbon to thorium-234 ratios in the ocean and their impact on the application of ^{234}Th as a POC flux proxy. *Marine Chemistry*, *100*(3–4), 213–233. https://doi.org/10.1016/j.marchem.2005.10.013

Buesseler, K. O., Benitez-Nelson, C. R., Roca-Martí, M., Wyatt, A., Resplandy, L., Clevenger, S. J., et al. (2020). High-resolution spatial and temporal measurements of particulate organic carbon flux using thorium-234 in the northeast Pacific Ocean during the EXport Processes in the Ocean from RemoTe Sensing field campaign. *Elementa: Science of the Anthropocene*, *8*(1), 030. https://doi.org/10.1525/elementa.030

Buesseler, K. O., Boyd, P. W., Black, E. E., & Siegel, D. A. (2020). Metrics that matter for assessing the ocean biological carbon pump. *Proceedings of the National Academy of Science*, *117*(18), 9679–9687. https://doi.org/10.1073/pnas.1918114117

Ceballos-Romero, E., Le Moigne, F. A. C., Henson, S., Marsay, C. M., Sanders, R. J., García-Tenorio, R., & Villa-Alfageme, M. (2016). Influence of bloom dynamics on Particle Export Efficiency in the North Atlantic: A comparative study of radioanalytical techniques and sediment traps. *Marine Chemistry*, *186*, 198–210. https://doi.org/10.1016/j.marchem.2016.10.001

Charette, M. A., & Moore, W. S. (2023a). *Water column dissolved radium-226 and radium-228 from Leg 1 (Seattle, WA to Hilo, HI) of the US GEOTRACES Pacific Meridional Transect (PMT) cruise (GP15, RR1814) on R/V Roger Revelle from September to October 2018*. Biological and Chemical Oceanography Data Management Office (BCO-DMO). (Version 3) Version Date 2023-10-02. https://doi.org/10.26008/1912/bco-dmo.825891.3

Charette, M. A., & Moore, W. S. (2023b). *Water column dissolved radium-226 and radium-228 from Leg 2 (Hilo, HI to Papeete, French Polynesia) of the US GEOTRACES Pacific Meridional Transect (PMT) cruise (GP15, RR1815) on R/V Roger Revelle from October to November 2018*. Biological and Chemical Oceanography Data Management Office (BCO-DMO). (Version 3) Version Date 2023-10-02. https://doi.org/10.26008/1912/bco-dmo.825947.3

Charette, M. A., Morris, P. J., Henderson, P. B., & Moore, W. S. (2015). Radium isotope distributions during the US GEOTRACES North Atlantic cruises. *Marine Chemistry*, *177*, 184–195. https://doi.org/10.1016/j.marchem.2015.01.001

Chmiel, R., Lanning, N., Laubach, A., Lee, J.-M., Fitzsimmons, J., Hatta, M., et al. (2022). Major processes of the dissolved cobalt cycle in the North and equatorial Pacific Ocean. *Biogeosciences*, *19*(9), 2365–2395. https://doi.org/10.5194/bg-19-2365-2022

Choi, H. Y., Stewart, G., Lomas, M. W., Kelly, R. P., & Moran, S. B. (2014). Linking the distribution of ^{210}Po and ^{210}Pb with plankton community along Line P, Northeast Subarctic Pacific. *Journal of Environmental Radioactivity*, *138*, 390–401. https://doi.org/10.1016/j.jenvrad.2014.02.009

Chuang, C.-Y., Santschi, P. H., Ho, Y.-F., Conte, M. H., Guo, L., Schumann, D., et al. (2013). Role of biopolymers as major carrier phases of Th, Pa, Pb, Po, and Be radionuclides in settling particles from the Atlantic Ocean. *Marine Chemistry*, *157*, 131–143. https://doi.org/10.1016/j.marchem.2013.10.002

Chung, Y., & Craig, H. (1983). ^{210}Pb in the Pacific: The GEOSECS measurements of particulate and dissolved concentrations. *Earth and Planetary Science Letters*, *65*(2), 406–432. https://doi.org/10.1016/0012-821x(83)90179-6

Chung, Y., & Finkel, R. (1988). ^{210}Po in the western Indian Ocean: Distributions, disequilibria and partitioning between the dissolved and particulate phases. *Earth and Planetary Science Letters*, *88*(3–4), 232–240. https://doi.org/10.1016/0012-821x(88)90080-5

Chung, Y., Finkel, R., Bacon, M. P., Cochran, J. K., & Krishnaswami, S. (1983). Intercomparison of ^{210}Pb measurements at GEOSECS station 500 in the northeast Pacific. *Earth and Planetary Science Letters*, *65*(2), 393–405. https://doi.org/10.1016/0012-821X(83)90178-4

Chung, Y., & Wu, T. (2005). Large ^{210}Po deficiency in the northern South China Sea. *Continental Shelf Research*, *25*(10), 1209–1224. https://doi.org/10.1016/j.csr.2004.12.016

Cochran, J. K. (1992). The Oceanic Chemistry of the Uranium and Thorium-Series Nuclides. In M. Ianovich & R. Harmon (Eds.), *Uranium Series Disequilibrium-Application to Environmental Problems: Applications to Earth, Marine, and Environmental Sciences* (2nd ed., pp. 334–395). Oxford Press.

Cochran, J. K., Bacon, M. P., Krishnaswami, S., & Turekian, K. K. (1983). ^{210}Po and ^{210}Pb distributions in the central and eastern Indian Ocean. *Earth and Planetary Science Letters*, *65*(2), 433–452. https://doi.org/10.1016/0012-821X(83)90180-2

Cochran, J. K., & Kadko, D. C. (2022a). *Activities of ^{210}Po and ^{210}Pb in aerosol samples collected on Leg 1 (Seattle, WA to Hilo, HI) of the US GEOTRACES Pacific Meridional Transect (PMT) cruise (GP15, RR1814) on R/V Roger Revelle from September to October 2018*. Biological and Chemical Oceanography Data Management Office (BCO-DMO). (Version 1) Version Date 2022-08-17. https://doi.org/10.26008/1912/bco-dmo.878689.1

Cochran, J. K., & Kadko, D. C. (2022b). *Activities of ^{210}Po and ^{210}Pb in aerosol samples collected on Leg 2 (Hilo, HI to Papeete, French Polynesia) of the US GEOTRACES Pacific Meridional Transect (PMT) cruise (GP15, RR1815) on R/V Roger Revelle from October to November 2018*. Biological and Chemical Oceanography Data Management Office (BCO-DMO). (Version 1) Version Date 2022-08-17. https://doi.org/10.26008/1912/bco-dmo.878703.1

Cochran, J. K., & Masqué, P. (2003). Short-lived U/Th series radionuclides in the ocean: Tracers for Scavenging rates, export fluxes and particle dynamics. *Reviews in Mineralogy and Geochemistry*, *52*(1), 461–492. https://doi.org/10.2113/0520461

Cochran, J. K., McKibbin-Vaughan, T., Dornblaser, M. M., Hirschberg, D., Livingston, H. D., & Buesseler, K. O. (1990). ^{210}Pb scavenging in the North Atlantic and North Pacific Oceans. *Earth and Planetary Science Letters*, *97*(3), 332–352. https://doi.org/10.1016/0012-821X(90)90050-8

Cochran, J. K., & Stephens, M. (2023a). *Dissolved and total water column ^{210}Po and ^{210}Pb from samples collected on Leg 1 (Seattle, WA to Hilo, HI) of the US GEOTRACES Pacific Meridional Transect (PMT) cruise (GP15, RR1814) on R/V Roger Revelle from September to October 2018*. Biological and Chemical Oceanography Data Management Office (BCO-DMO). (Version 1) Version Date 2023-01-06. https://doi.org/10.26008/1912/bco-dmo.883724.1

Cochran, J. K., & Stephens, M. (2023b). *Dissolved and total water column ^{210}Po and ^{210}Pb from samples collected on Leg 2 (Hilo, HI to Papeete, French Polynesia) of the US GEOTRACES Pacific Meridional Transect (PMT) cruise (GP15, RR1815) on R/V Roger Revelle from October to November 2018*. Biological and Chemical Oceanography Data Management Office (BCO-DMO). (Version 1) Version Date 2023-01-31. https://doi.org/10.26008/1912/bco-dmo.883797.1

Cochran, J. K., & Stephens, M. (2023c). *Activities of ^{210}Po and ^{210}Pb on particles in two size classes obtained by in situ pumping on Leg 1 (Seattle, WA to Hilo, HI) of the US GEOTRACES Pacific Meridional Transect (PMT) cruise (GP15, RR1814) on R/V Roger Revelle from September to October 2018*. Biological and Chemical Oceanography Data Management Office (BCO-DMO). (Version 1) Version Date 2023-03-23. https://doi.org/10.26008/1912/bco-dmo.892348.1

Cochran, J. K., & Stephens, M. (2023d). *Activities of ^{210}Po and ^{210}Pb on particles in two size classes obtained by in situ pumping on Leg 2 (Hilo, HI to Papeete, French Polynesia) of the US GEOTRACES Pacific Meridional Transect (PMT) cruise (GP15, RR1815) on R/V Roger Revelle*

from Oct-Nov 2018. Biological and Chemical Oceanography Data Management Office (BCO-DMO). (Version 1) Version Date 2023-03-23. https://doi.org/10.26008/1912/bco-dmo.892360.1

Craig, H., Krishnaswami, S., & Somayajulu, B. L. K. (1973). ^{210}Pb-^{226}Ra: Radioactive disequilibrium in the deep sea. *Earth and Planetary Science Letters*, *17*(2), 295–305. https://doi.org/10.1016/0012-821x(73)90194-5

Fisher, N. S., Burns, K. A., Cherry, R. D., & Heyraud, M. (1983). Accumulation and cellular distribution of ^{241}Am, ^{210}Po and ^{210}Pb in two marine algae. *Marine Ecology Progress Series*, *11*, 233–237. https://doi.org/10.3354/meps011233

Fisher, N. S., Teyssie, J.-L., Krishnaswami, S., & Baskaran, M. (1987). Accumulation of Th, Pb, U, and Ra in marine phytoplankton and its geochemical significance. *Limnology and Oceanography*, *32*(1), 131–142. https://doi.org/10.4319/lo.1987.32.1.0131

Fleer, A. P., & Bacon, M. P. (1984). Determination of ^{210}Pb and ^{210}Po in seawater and marine particulate matter. *Nuclear Instruments and Methods Physical Research*, *223*(2–3), 243–249. https://doi.org/10.1016/0167-5087(84)90655-0

Flynn, W. W. (1968). The determination of low levels of polonium-210 in environmental materials. *Analalytica Chimica Acta*, *43*, 221–227. https://doi.org/10.1016/S0003-2670(00)89210-7

Friedrich, J., & Rutgers van der Loeff, M. M. (2002). A two-tracer (^{210}Po–^{234}Th) approach to distinguish organic carbon and biogenic silica export flux in the Antarctic Circumpolar Current. *Deep-Sea Research Part I Oceanographic Research Paers*, *49*(1), 101–120. https://doi.org/10.1016/S0967-0637(01)00045-0

Hayes, C. T., Black, E. E., Anderson, R. F., Baskaran, M., Buesseler, K. O., Charette, M. A., et al. (2018). Flux of particulate elements in the North Atlantic Ocean constrained by multiple radionuclides. *Global Biogeochemical Cycles*, *32*(12), 1738–1758. https://doi.org/10.1029/2018GB005994

Honeyman, B. D., & Santschi, P. H. (1989). A Brownian-pumping model for oceanic trace metal scavenging: Evidence from Th isotopes. *Journal of Marine Research*, *47*(4), 951–992. https://doi.org/10.1357/002224089785076091

Hong, G.-H., Kim, Y.-I., Baskaran, M., Kim, S.-H., & Chung, C.-S. (2008). Distribution of ^{210}Po and export of organic carbon from the euphotic zone in the Southwestern East Sea (Sea of Japan). *Journal of Oceanography*, *64*(2), 277–292. https://doi.org/10.1007/s10872-008-0022-4

Hong, G. H., Park, S. K., Baskaran, M., Kim, S. H., Chung, C. S., & Lee, S. H. (1999). Lead-210 and polonium-210 in the winter well-mixed turbid waters in the mouth of the Yellow Sea. *Continental Shelf Research*, *19*(8), 1049–1064. https://doi.org/10.1016/s0278-4343(99)00011-4

Horowitz, E., Cochran, J. K., Bacon, M., & Hirschberg, D. (2020). ^{210}Po and ^{210}Pb distributions during a phytoplankton bloom in the North Atlantic: Implications for POC export. *Deep-Sea Research Part I Oceanogaphic. Research Papers*, *164*, 103339. https://doi.org/10.1016/j.dsr.2020.103339

Kadko, D. (1993). Excess ^{210}Po and nutrient recycling within the California Coastal Transition Zone. *Journal of Geophysical Research*, *15*(C1), 857–864. https://doi.org/10.1029/92jc01932

Kenyon, J. A. (2022). *Anthropogenic and natural radioisotopes as tracers for contaminant sources and particulate fluxes* (PhD thesis) (p. 176). Woods Hole Oceanographic Institution.

Kim, G., & Church, T. M. (2001). Seasonal biogeochemical fluxes of ^{234}Th and ^{210}Po in the Upper Sargasso Sea: Influence from atmospheric iron deposition. *Global Biogeochemical Cycles*, *15*(3), 651–661. https://doi.org/10.1029/2000GB001313

Lam, P. J., Ohnemus, D. C., & Auro, M. F. (2015). Size-fractionated major particle composition and concentrations from the US GEOTRACES North Atlantic Zonal Transect. *Deep-Sea Researcch II*, *116*, 303–320. https://doi.org/10.1016/j.dsr2.2014.11.020

Lanning, N. T., Jiang, S., Amaral, V. J., Mateos, K., Steffen, J. M., Lam, P. J., et al. (2023). Isotopes illustrate vertical transport of anthropogenic Pb by reversible scavenging within Pacific Ocean particle veils. *Proceedings of the National Academy of Science*, *120*(23), e2219688120. https://doi.org/10.1073/pnas.2219688120

Lee, H. M., Hong, G. H., Baskaran, M., Kim, S. H., & Kim, Y. I. (2014). Evaluation of plating conditions for the recovery of ^{210}Po on a Ag planchet. *Applied Radiation and Isotopes*, *90*, 170–176. https://doi.org/10.1016/j.apradiso.2014.03.025

Lemaitre, N., Planchon, F., Planquette, H., Dehairs, F., Fonseca-Batista, D., Roukaerts, A., et al. (2018). High variability of particulate organic carbon export along the North Atlantic GEOTRACES section GA01 as deduced from ^{234}Th fluxes. *Biogeosciences*, *15*(21), 6417–6437. https://doi.org/10.5194/bg-15-6417-2018

LeMoigne, F. A. C., Villa-Alfageme, M., Sanders, R. J., Marsay, C., Henson, S., & García-Tenorio, R. (2013). Export of organic carbon and biominerals derived from ^{234}Th and ^{210}Po at the Porcupine Abyssal Plain. *Deep Sea Research Part I: Oceanographic Research Papers*, *72*, 88–101. https://doi.org/10.1016/j.dsr.2012.10.010

Li, Y.-H., Burkhardt, L., Buchholtz, M., O'Hara, P., & Santschi, P. H. (1984). Partition of radiotracers between suspended particles and seawater. *Geochimica et Cosmochimica Acta*, *48*(10), 2011–2019. https://doi.org/10.1016/0016-7037(84)90382-x

Lin, P., Xu, C., Xing, W., & Santschi, P. H. (2021). Molecular level characterization of diatom and coccolithophore-associated biopolymers that are binding ^{210}Pb and ^{210}Po in seawater. *Frontiers in Marine Science*, *8*, 703503. https://doi.org/10.3389/fmars.2021.703503

Marsay, C. M., Kadko, D., Landing, W. M., & Buck, C. S. (2022). Bulk aerosol trace element concentrations and deposition fluxes during the US GEOTRACES GP15 Pacific Meridional Transect. *Global Biogeochemical Cycles*, *36*(2), e2021GB007122. https://doi.org/10.1029/2021GB007122

Murnane, R. J., Cochran, J. K., Buesseler, K. O., & Bacon, M. P. (1996). Least-squares estimates of thorium, particle and nutrient cycling rate constants from the JGOFS North Atlantic Bloom Experiment. *Deep-Sea Research I*, *43*(2), 239–258.

Murray, J. W., Paul, B., Dunne, J. P., & Chapin, T. (2005). ^{234}Th, ^{210}Pb, ^{210}Po and stable Pb in the central equatorial Pacific: Tracers for particle cycling. *Deep-Sea Research I*, *52*(11), 2109–2139. https://doi.org/10.1016/j.dsr.2005.06.016

Murray, J. W., Young, J., Newton, J., Dunne, J., Chapin, T., Paul, B., & McCarthy, J. J. (1996). Export flux of particulate organic carbon from the central equatorial Pacific determined using a combined drifting trap-^{234}Th approach. *Deep-Sea Research II*, *43*(4–6), 1095–1132. https://doi.org/10.1016/0967-0645(96)00036-7

Niedermiller, J. (2017). *Comparison of the scavenging intensity, remineralization and residence time of ^{210}Po and ^{210}Pb at key interfaces (biotic, sediment-water and hydrothermal) along the East Pacific Zonal Transect* (Masters Thesis) (p. 120). Wayne State University Theses.

Niedermiller, J., & Baskaran, M. (2019). Comparison of the scavenging intensity, remineralization and residence time of ^{210}Po and ^{210}Pb at key zones (biotic, sediment-water and hydrothermal) along the East Pacific GEOTRACES transect. *Journal of Environmental Radioactivity*, *198*, 165–188. https://doi.org/10.1016/j.jenvrad.2018.12.016

Nozaki, Y., Dobashi, F., Kato, Y., & Yamamoto, Y. (1998). Distribution of Ra isotopes and the ^{210}Pb and ^{210}Po balance in surface waters of the mid Northern Hemisphere. *Deep Sea Research Part I: Oceanographic Research Papers*, *45*(8), 1263–1284.

Nozaki, Y., Thomson, J., & Turekian, K. K. (1976). The distribution of ^{210}Pb and ^{210}Po in the surface waters of the Pacific Ocean. *Earth and Planetary Science Letters*, *32*(2), 304–312. https://doi.org/10.1016/0012-821x(76)90070-4

Nozaki, Y., & Tsunogai, S. (1976). ^{226}Ra, ^{210}Pb and ^{210}Po disequilibria in the western North Pacific. *Earth and Planetary Science Letters*, *32*(2), 313–321. https://doi.org/10.1016/0012-821x(76)90071-6

Nozaki, Y., Turekian, K. K., & Von Damm, K. (1980). ^{210}Pb in GEOSECS water profiles from the North Pacific. *Earth and Planetary Science Letters*, *49*(2), 393–400. https://doi.org/10.1016/0012-821X(80)90081-3

Nozaki, Y., Zhang, J., & Takeda, A. (1997). ^{210}Pb and ^{210}Po in the equatorial Pacific and the Bering Sea: The effects of biological productivity and boundary scavenging. *Deep-Sea Research Part II Toical. Studies in Oceanography*, *44*(9–10), 2203–2220. https://doi.org/10.1016/S0967-0645(97)00024-6

Owens, S. A., Pike, S., & Buesseler, K. O. (2015). Thorium-234 as a tracer of particle dynamics and upper ocean export in the Atlantic Ocean. *Deep Sea Research Part II: Topical Studies in Oceanography*, *116*, 42–59. https://doi.org/10.1016/j.dsr2.2014.11.010

Passow, U., & Carlson, C. A. (2012). The biological pump in a high CO_2 world. *Marine Ecology Progress Series*, *470*, 249–271. https://doi.org/10.3354/meps09985

Planaj, D., & Baskaran, M. (2024). Inventory-based evaluation of ^{210}Po-^{210}Pb-^{226}Ra disequilibria in deep oceans and new insights on their utility as biogeochemical tracers: A global data synthesis of research over six decades. *Earth-Science Reviews*, *252*, 104759. https://doi.org/10.1016/j.earscirev.2024.104759

Rama, Koide, M., & Goldberg, E. D. (1961). Lead-210 in natural waters. *Science*, *134*(3472), 98–99. https://doi.org/10.1126/science.134.3472.98

Rigaud, S., Puigcorbé, V., Cámara-Mor, P., Casacuberta, N., Roca-Martí, M., Garcia-Orellana, J., et al. (2013). A methods assessment and recommendations for improving calculations and reducing uncertainties in the determination of ^{210}Po and ^{210}Pb activities in seawater. *Limnology and Oceanography: Methods*, *11*(10), 561–571. https://doi.org/10.4319/lom.2013.11.561

Rigaud, S., Stewart, G., Baskaran, M., Marsan, D., & Church, T. (2015). ^{210}Po and ^{210}Pb distribution, dissolved-particulate exchange rates, and particulate export along the North Atlantic US GEOTRACES GA03 section. *Deep Sea Research Part II: Topical Studies in Oceanography*, *116*, 60–78. https://doi.org/10.1016/j.dsr2.2014.11.003

Roca-Martí, M., Puigcorbé, V., Castrillejo, M., Casacuberta, N., Garcia-Orellana, J., Cochran, J. K., & Masqué, P. (2021). Quantifying ^{210}Po/^{210}Pb disequilibrium in Seawater: A comparison of two precipitation methods with differing results. *Frontiers in Maine. Science*, *8*, 684484. https://doi.org/10.3389/fmars.2021.684484

Roca-Martí, M., Puigcorbé, V., Rutgers van der Loeff, M. M., Katlein, C., Fernández-Méndez, M., Peeken, I., & Masqué, P. (2016). Carbon export fluxes and export efficiency in the central Arctic during the record sea-ice minimum in 2012: A joint ^{234}Th/^{238}U and ^{210}Po/^{210}Pb study. *Journal of Geophysical Research: Oceans*, *121*(7), 5030–5049. https://doi.org/10.1002/2016JC011816

Sarin, M. M., Kim, G., & Church, T. M. (1999). ^{210}Po and ^{210}Pb in the South-equatorial Atlantic: Distribution and disequilibrium in the upper 500 m. *Deep Sea Research Part II: Topical Studies in Oceanography*, *46*(5), 907–917. https://doi.org/10.1016/S0967-0645(99)00008-9

Shimmield, G. B., Ritchie, G. D., & Fileman, T. W. (1995). The impact of marginal ice zone processes on the distribution of ^{210}Pb, ^{210}Po and ^{234}Th and implications for new production in the Bellingshausen Sea, Antarctica. *Deep Sea Research Part II: Topical Studies in Oceanography*, *42*(4–5), 1313–1335. https://doi.org/10.1016/0967-0645(95)00071-W

Somayajulu, B. L. K., & Craig, H. (1976). Particulate and soluble ^{210}Pb activities in the deep sea. *Earth and Planetary Science Letters*, *32*(2), 268–276. https://doi.org/10.1016/0012-821x(76)90067-4

Spencer, D. W., Bacon, M. P., & Brewer, P. G. (1981). Models of the distribution of ^{210}Pb in a section across the North Equatorial Atlantic Ocean. *Journal of Marine Research*, *39*, 119–138.

Stewart, G., Cochran, J. K., Miquel, J. C., Masqué, P., Szlosek, J., Rodriguez y Baena, A. M., et al. (2007). Comparing POC export from ^{234}Th/^{238}U and ^{210}Po/^{210}Pb disequilibria with estimates from sediment traps in the northwest Mediterranean. *Deep Sea Research Part I: Oceanographic Research Papers*, *54*(9), 1549–1570. https://doi.org/10.1016/j.dsr.2007.06.005

Stewart, G., & Fisher, N. S. (2003a). Bioaccumulation of polonium-210 in marine copepods. *Limnology and Oceanography*, *48*(5), 2011–2019. https://doi.org/10.4319/lo.2003.48.5.2011

Stewart, G., & Fisher, N. S. (2003b). Experimental studies on the accumulation of polonium- 210 by marine phytoplankton. *Limnology and Oceanography*, *48*(3), 1193–1201. https://doi.org/10.4319/lo.2003.48.3.1193

Stewart, G., Moran, S. B., & Lomas, M. W. (2010). Seasonal POC fluxes at BATS estimated from ^{210}Po deficits. *Deep Sea Research Part I: Oceanographic Research Papers*, *57*, 113–124. https://doi.org/10.1016/j.dsr.2009.09.007

Stewart, G. M., Fowler, S. W., Teyssié, J.-L., Cotret, O., Cochran, J. K., & Fisher, N. S. (2005). Contrasting transfer of polonium-210 and lead-210 across three trophic levels in marine plankton. *Marine Ecology Progress Series*, *290*, 27–33. https://doi.org/10.3354/meps290027

Tang, Y., Lemaitre, N., Castrillejo, M., Roca-Martí, M., Pere Masqué, P., & Stewart, G. (2019). The export flux of particulate organic carbon derived from ^{210}Po/^{210}Pb disequilibria along the North Atlantic GEOTRACES GA01 transect: GEOVIDE cruise. *Biogeosciences*, *16*(2), 309–327. https://doi.org/10.5194/bg-16-309-2019

Tang, Y., & Stewart, G. (2019). The ^{210}Po/^{210}Pb method to calculate particle export: Lessons learned from the results of three GEOTRACES transects. *Marine Chemistry*, *217*, 103692. https://doi.org/10.1016/j.marchem.2019.103692

Thomson, J., & Turekian, K. K. (1976). ^{210}Po and ^{210}Pb distributions in ocean water profiles from the Eastern South Pacific. *Earth and Planetary Science Letters*, *32*(2), 297–303. https://doi.org/10.1016/0012-821X(76)90069-8

Tsunogai, S., & Nozaki, Y. (1971). Lead-210 and polonium-210 in surface water of the Pacific. *Geochemical Journal*, *5*(4), 165–173. https://doi.org/10.2343/geochemj.5.165

Turekian, K. K., Graustein, W. C., & Cochran, J. K. (1989). Lead-210 in the SEAREX program: An aerosol tracer across the Pacific. *Chemical Oceanography*, *10*, 51–81.

Turekian, K. K., Nozaki, Y., & Benninger, L. K. (1977). Geochemistry of atmospheric radon and radon products. *Annual Review of Earth and Planetary Sciences*, *5*(1), 227–255. https://doi.org/10.1146/annurev.ea.05.050177.001303

Verdeny, E., Masqué, P., Garcia-Orellana, J., Hanfland, C., Cochran, J. K., & Stewart, G. (2009). POC export from ocean surface waters using ^{234}Th/^{238}U and ^{210}Po/^{210}Pb disequilibria: A review of the use of two radiotracer pairs. *Deep-Sea Research Part II Topical Studies in. Oceanography*, *56*(18), 1502–1518. https://doi.org/10.1016/j.dsr2.2008.12.018

Verdeny, E., Masqué, P., Maiti, K., Garcia-Orellana, J., Bruach, J. M., & Benitez-Nelson, C. (2008). Particle export within cyclonic Hawaiian lee eddies derived from ^{210}Pb–^{210}Po disequilibrium. *Deep Sea Research Part II: Topical Studies in Oceanography*, *55*(10–13), 1461–1472. https://doi.org/10.1016/j.dsr2.2008.02.009

Wei, C.-L., Chia, C.-Y., Chou, W.-C., & Lee, W.-H. (2017). Sinking fluxes of ^{210}Pb and ^{210}Po in the deep basin of the northern South China Sea. *Journal of Environmental Radioactivity*, *174*, 45–53. https://doi.org/10.1016/j.jenvrad.2016.05.026

Wei, Z., Cochran, J. K., Horowitz, E., Fitzgerald, P., Heilbrun, C., Kadko, D., et al. (2022). ^{210}Pb and ^{7}Be as coupled flux and source tracers for aerosols in the Pacific Ocean. *Global Biogeochemical Cycles*, *36*(8), e2022GB007378. https://doi.org/10.1029/2022GB007378

Westberry, T., Behrenfeld, D., Siegel, D., & Boss, E. (2008). Carbon-based primary productivity modeling with vertically resolved photoacclimation. *Global Biogeochemical Cycles*, *22*(2), GB2024. https://doi.org/10.1029/2007GB003078